An aerodynamic roughness length map derived from extended martian rock abundance data

Eric Hébrard, Constantino Listowski, P. Coll, B. Marticorena, G. Bergametti, Anni Määttänen, Franck Montmessin, François Forget

An aerodynamic roughness length map derived from extended Martian rock abundance data

E. Hébrard,[1,2,3] C. Listowski,[2,4] P. Coll,[1] B. Marticorena,[1] G. Bergametti,[1] A. Määttänen,[2] F. Montmessin,[2] and F. Forget[4]

Received 23 August 2011; revised 27 February 2012; accepted 1 March 2012; published 27 April 2012.

[1] Many boundary layer processes simulated within a Mars General Circulation Model (MGCM), including the description of the processes controlling dust rising from the Martian surface, are highly sensitive to the aerodynamic roughness length z_0. On the basis of rock-size frequency distributions inferred from different Martian landing sites and Earth analog sites, we have first established that lognormal-modeled rock-size frequency distributions are able to reproduce correctly the observed Martian rock populations. We have validated the hypothesis that the rock abundance ζ of a given area could be estimated at a first order from its thermophysical properties, namely its thermal inertia I and its albedo α. We have demonstrated the possibility of using rock abundance ζ to estimate the roughness density λ on Mars and to retrieve subsequently the aerodynamic roughness length by using semi-empirical relationships based on terrestrial wind-tunnel and field measurements. By combining our methodology with remote sensing measurements of the Thermal Emission Spectrometer aboard Mars Global Surveyor, we have derived a global map of the aeolian aerodynamic roughness length with a $1/8^\circ \times 1/8^\circ$ resolution over the entire Martian surface. Contrary to what is often assumed, the Martian aeolian aerodynamic roughness length is spatially highly heterogeneous. At the fullest resolution, the Martian aerodynamic roughness length varies from 10^{-3} cm to 2.33 cm. About 84% of the Martian surface seems to be characterized by an aeolian aerodynamic roughness length value lower than 1 cm, the spatially uniform value that most of the MGCMs simulations have assumed recently. Since the aerodynamic roughness length z_0 is a key parameter in deriving the erosion threshold wind velocities, we anticipate a significant impact of our findings on the efficiencies for lifting dust in future MGCMs.

Citation: Hébrard, E., C. Listowski, P. Coll, B. Marticorena, G. Bergametti, A. Määttänen, F. Montmessin, and F. Forget (2012), An aerodynamic roughness length map derived from extended Martian rock abundance data, *J. Geophys. Res.*, *117*, E04008, doi:10.1029/2011JE003942.

1. Introduction

[2] Dust emission on Mars can result from large-scale dust storms as well as from smaller dust events, such as dust-raising convective vortices (dust devils). According to *Cantor et al.*'s [2001] classification, regional dust storms are defined as events covering an area $\geq 1.6 \times 10^6$ km^2 over a duration >3 sols whereas local dust storms either cover an area $< 1.6 \times 10^6$ km^2 or persist <3 sols. These regional- or local-scale dust storms are susceptible to combine and evolve toward global dust storms leading to global obscuration. Identified up to now as bright spots, such active dust-raising regions appear to develop over the lifetime of the global storm [*Martin*, 1974, 1976; *Zurek*, 1982; *Cantor*, 2007]. These regions end up producing and sustaining a dust haze that extends upwards to reach altitudes of about 65–70 km, longitudinally encircles the planet, and latitudinally obscures one or both hemispheres [*Cantor*, 2007]. On the basis of spacecraft and Earth-based observations, these different dust storm events have been spotted in the Hellas and Argyre basins, Noachis, Amazonis, Hellespontus, Syrtis, Thaumasia, Solis, Claritas, Meridiani and Chryse regions. The local or regional dust storms typically appear during one or two seasons every year whereas the global dust storms are thought to occur only once every two to three Martian years, around perihelion during the southern spring and summer season

[1]Laboratoire Interuniversitaire des Systèmes Atmosphériques, UMR CNRS 7583, Université Paris Est Créteil et Université Paris Diderot, Institut Pierre Simon Laplace, C.M.C., Créteil, France.
[2]Laboratoire Atmosphères, Milieux, Observations Spatiales, UMR CNRS 8190, Université de Versailles Saint Quentin en Yvelines et Université Pierre et Marie Curie, Institut Pierre Simon Laplace, Guyancourt, France.
[3]Now at Laboratoire d'Astrophysique de Bordeaux, UMR CNRS 5804, Université Bordeaux 1, Observatoire Aquitain des Sciences de l'Univers, Floirac, France.
[4]Laboratoire de Météorologie Dynamique, UMR CNRS 8539, Université Pierre et Marie Curie, Institut Pierre Simon Laplace, Paris, France.

0148-0227/12/2011JE003942

[*Zurek and Martin*, 1993]. For a nonglobal dust storm year, the annual dust flux lifted by both local and regional dust storms and by dust devils has been estimated on Mars to range between 7.3×10^{11} and 10.8×10^{11} kg per Martian year [*Cantor et al.*, 2001, 2006; *Whelley and Greeley*, 2008]. One global dust storm, however, can raise a comparable amount of dust over a far shorter period. For example, the 1977b global storm was estimated to have raised 4.3×10^{11} kg only during a fraction of a Martian year (Ls $\sim$ 268°–350°) [*Martin*, 1995], quite comparable to what regular Martian dust storm activity may lift in one full Martian year.

[3] The global magnitude of natural dust injected in the Earth's atmosphere is currently suggested to range between 10×10^{11} and 26×10^{11} kg per standard year [*Zender et al.*, 2004; *Cakmur et al.*, 2006]. By comparing the globally and long-term time-averaged dust lifting on both planets, Mars is found to be up to 3 times "dustier" than Earth. Terrestrial dust events do not occur on such a massive scale, despite surface wind stresses being generally larger than those on Mars. It is mainly because only a small fraction of Earth's surface, unlike Mars', is covered with dust - the remainder being water, ice or non-erodible soil (with or without vegetation cover). Any dust storm beginning within a desertified area on Earth (e.g. Sahara or eastern Asian deserts) will rapidly run out of source particles when it moves over dust-free surfaces. Moreover, the presence of more water in Earth's atmosphere means that dust particles are scavenged more rapidly by precipitation.

[4] The tremendous amounts of atmospheric dust lifted during Martian dust events strongly absorb and scatter short-wave solar radiation, but also absorb and emit long-wave radiation, which results in a considerable impact on the radiative heating and the atmospheric thermal structure, the global circulation patterns and thus the climate in general [*Haberle et al.*, 1982; *Murphy et al.*, 1995; *Wilson*, 1997]. The potential for such large quantities of dust to appear in some regions, in only a broadly predictable manner, therefore makes it a major contributor to atmospheric variability on Mars. Thus, a good representation of the dust cycle is an important component of any model intended to recreate the observed behavior of the atmospheric circulation [*Newman et al.*, 2002a].

[5] However, even the latest models generally fail in simulating the variability of the dust distribution on Mars because of limited spatial resolutions and simplistic and/or inaccurate dust lifting parameterizations. Detailed dust emission schemes have recently been included in General Circulation Models to simulate the interactive lifting and transport of radiatively active dust [*Newman et al.*, 2002a; *Basu and Richardson*, 2004; *Kahre et al.*, 2005, 2006] and to forecast the spatial and temporal variability of dust storms [*Newman et al.*, 2002b, 2005; *Basu et al.*, 2006; *Spiga and Lewis*, 2010] and atmospheric dust particle sizes [*Kahre et al.*, 2008]. The emission schemes used in these modeling studies [*Bagnold*, 1954; *White*, 1979; *Greeley and Iversen*, 1985; *Westphal et al.*, 1987; *Raupach*, 1991; *Gillette et al.*, 1998; *Shao*, 2001] provide a physical description of the main processes involved in the wind stress-driven dust emission: the erosion threshold, the saltation fluxes (of larger sand-sized particles) and the dust emission by sandblasting processes (in which sand particles sendoff dust). The erosion threshold friction velocity u^t_{drag}, which is the minimal wind friction velocity u_{drag} required to initiate the emission of mineral dust by aeolian erosion, is one of the key parameters to describe these emissions. Indeed, the dust emission frequency is determined by the number of times the wind friction velocity exceeds the erosion threshold friction velocity while the dust emission intensity depends on the amount by which this threshold is exceeded. This erosion threshold is mainly controlled by a handful of surface features (surface roughness, soil particle size distribution, interparticle cohesion, etc.), among which the aeolian aerodynamic roughness length z_0 is one of the main influencing factors. It raises two opposing effects. On the one hand, z_0 determines, for a given wind velocity profile $u(z)$, the total wind friction velocity $u_{drag} = ku(z)/\ln\left(\frac{z}{z_0}\right)$ [*Priestley*, 1959] (with k the Von Kármán constant): u_{drag} increases with z_0. On the other hand, z_0 reflects the effect of the non-erodible surface roughness elements on this air flow momentum [*Schlicting*, 1936]. It accounts therefore for the wind shear stress partition between these roughness elements and the intervening smooth surface: the fraction of wind friction velocity u_{drag} actually available for lifting dust decreases with z_0.

[6] Even so, these surface features, and particularly the aeolian aerodynamic roughness length, are still poorly documented in the literature and their spatial variations have not been fully investigated yet on Mars. Mars General Circulation Models (MGCMs) simulations [*Newman et al.*, 2002a, 2002b, 2005; *Kahre et al.*, 2005, 2006, 2008; *Spiga and Lewis*, 2010] have thus often assumed a spatially uniform aerodynamic roughness length either within the 0.1–1 cm range estimated for the Viking landing sites [*Sutton et al.*, 1978] or even outside, as it is the case in the Geophysical Fluid Dynamics Laboratory Mars GCM, which implements a uniform z_0 = 16.62 cm [*Wilson and Hamilton*, 1996]. However, a few MGCMs (e.g. the MarsWRF GCM described by *Richardson et al.* [2007]) do include a spatially variable roughness map as standard. *Heavens et al.* [2008] recently described some impact of running the Mars implementation of the Planetary Weather Research and Forecasting Model (MarsWRF) with two different spatially variable aerodynamic roughness length maps ranging from 2×10^{-2} cm to 16.62 cm and from 1 cm to 10 cm, respectively. Indeed, the aerodynamic roughness length is highly likely to vary spatially by 3 or 4 orders of magnitude as it is the case in terrestrial arid areas [see, e.g., *Marticorena et al.*, 2006, Table 7].

[7] In this study, we extended this approach to Mars. Our main objective was to perform an exhaustive and self-consistent mapping of the Martian aerodynamic roughness length as required for the estimation of mineral dust emissions at a global scale. A step-by-step description of the physical processes mandatory to model the wind erosion threshold is first detailed in section 2, and emphasizes the dual importance of the aerodynamic roughness length z_0. In section 3, we outline the methodology we relied on to retrieve remotely the aerodynamic roughness length z_0 of Martian terrains by using the geometry of the surface roughness elements and some simple assumptions over their shapes. We present in section 4 our extension to the whole Martian surface of the rock abundance data derived from the measurements of the Thermal Emission Spectrometer (TES) onboard Mars Global Surveyor (MGS) from the National Aeronautics and Space Agency (NASA). In section 5, we investigate the

relationships between the aerodynamic roughness length z_0, the roughness density λ, and the rock abundance ζ on Mars using rock size-frequency distributions inferred from different Martian landing sites and Earth analog sites. We finally apply in section 6 these relationships by generalizing them to the whole Martian surface and discuss our mapping of the aerodynamic roughness length z_0 with a spatial resolution down to $1/8^\circ \times 1/8^\circ$.

2. Physical Modeling of the Wind Erosion Threshold

[8] Dust emissions are the result of the aeolian action on erodible soil particles. From a physical point of view, the particles' motion initiated by wind is controlled by the forces acting on them. For a particle at rest, these forces are the weight, the interparticle cohesion forces, and the wind shear stress τ on the surface. Unlike the weight and the interparticle cohesion forces, the wind shear stress does not rely on the size and density of the particles being lifted but depends on the transfer of the wind energy to the erodible surface, which is in turn controlled by the presence of larger roughness elements on the surface. In combination, these factors determine the threshold friction velocity, u^t_{drag}, which must be exceeded by the friction velocity u_{drag} to initiate particle motion. The friction velocity u_{drag}, defined as $u_{drag} = \sqrt{\frac{\tau}{\rho}}$, is determined by the physics of the Surface Boundary-Layer where the wind profile is assumed logarithmic in neutral conditions [*Priestley*, 1959]:

$$u(z) \sim \frac{u_{drag}}{k} \ln\left(\frac{z}{z_0}\right) \tag{1}$$

where k is the Von Kármán constant, usually taken $\sim$0.4, z is the height above the surface and z_0 is the height at which velocities go to zero, called the aeolian aerodynamic roughness length. Therefore, for a given wind velocity profile $u(z)$:

$$u_{drag} \sim \frac{ku(z)}{\ln\left(\frac{z}{z_0}\right)} \tag{2}$$

Recent physical models have been developed to account for the influence of these surface characteristics on the dust emission, including in particular explicit parameterizations of the aeolian erosion threshold as a function of the surface roughness [*Marticorena and Bergametti*, 1995; *Shao et al.*, 1996]. *Marticorena and Bergametti* [1995] proposed an operational parameterization to describe the increase of the threshold wind friction velocity u^t_{drag} as a function of the aeolian aerodynamic roughness length z_0, which can be experimentally derived from vertical profiles of dynamical parameters (wind velocity, air temperature and pressure). Such a parametrization has been found to reproduce satisfactorily the thresholds of erosion measured on a variety of natural surfaces [*Marticorena et al.*, 1997].

2.1. Parameterization of the Threshold Friction Velocity

[9] Once the particle is in motion, its path depends on the balance between its weight acting downward and the opposite aerodynamic drag. The vertical extent of these trajectories defines three major types of grain motion, generally classified in relation to the particle size [*Bagnold*, 1941], which relates to the planet's gravity as well as on the typical density of the dust particles material. The medium-sized soil grains (60–2000 μm on Earth) are able to be lifted from the surface to a height of some tenths of centimeters but, as the drag is not sufficient to exceed the weight, they are carried downwind back to the surface. Such trajectories define a motion called "saltation". The larger and/or heavier particles (>2000 μm on Earth) cannot be lifted from the surface and roll along the surface in a motion called "creeping". Only the finest particles (<60 μm on Earth), or dust, are small enough to be transported upward by turbulent eddies, sometimes very far from their source. However, owing to interparticle cohesion forces, which are greatest for the smallest particle sizes, their threshold wind friction velocities are so high that their motion could not be initiated directly by the wind. On Earth, saltation is generally a necessary intermediate process for dust production, whereby dust particles are released by the impacts on the surface of the saltating particles [*Gomes et al.*, 1990; *Shao et al.*, 1993; *Alfaro et al.*, 1997]. As a result, the emission of mineral dust on Earth is especially efficient when both fine sand-sized particles ($\sim$100 μm) and aggregates of dust-sized particles are present in the soil. Wind tunnel experiments under simulated Martian conditions showed however that moderately rough surfaces on Mars may be able to lower the wind speeds needed to entrain dust-sized particles directly without saltation required [e.g., *White et al.*, 1997; *Greeley et al.*, 2000]. Since interparticle cohesion forces have not been measured on Mars, it remains however unclear exactly how close these wind tunnel experiments come to using the actual range of threshold friction velocities found on Mars.

2.2. Threshold Friction Velocity Versus Soil Particle Size

[10] The particle size dependence of the threshold wind friction velocity has been extensively investigated, both from a theoretical point of view and using wind-tunnel experiments [*Iversen and White*, 1982]. A theoretical formulation of the threshold friction velocity on a smooth surface u^{ts}_{drag} can be established by considering the equilibrium of the forces acting on a spherical loose particle at rest on a similar particle bed under an air flow stream. At the threshold of aeolian erosion, the aerodynamic forces due to the fluid equal the particle weight and the interparticle cohesion forces. Based on a similar analysis but ignoring the cohesion forces, *Bagnold* [1941] gave the following formulation for the threshold friction velocity on a smooth surface u^{ts}_{drag} :

$$u^{ts}_{drag} = A\sqrt{gD_p\frac{\rho_d - \rho}{\rho}} \tag{3}$$

where g is gravitational acceleration, ρ_d is particle density, D_p is particle diameter and ρ is atmospheric density. A is called the dimensionless threshold parameter and is expected to depend on the friction Reynolds number R_{*t}, which is defined at the erosion threshold as follows:

$$R_{*t} = u^{ts}_{drag} D_p/\nu \tag{4}$$

where ν is the atmospheric kinematic viscosity.

[11] Experimental data from *Bagnold* [1941] and *Chepil* [1945] confirmed this size dependence but also revealed an increase of the threshold friction velocity values for the smallest particles. This determines an optimum particle size ($\sim$80 μm in terrestrial conditions) for which the threshold friction velocity is minimum. *Iversen et al.* [1976] considered that interparticle cohesion forces could be responsible for this unexpected behavior of the finest particles. Based on a large set of measured threshold friction velocities obtained in wind tunnels and involving various particle densities (1.1 to 2.65 g.cm^{-3}) and diameters (37 to 673 μm) and low fluid density conditions (ρ_p/ρ_a ranging from 900 to 630,000), *Iversen and White* [1982] proposed new formulations to predict the saltation threshold friction velocity, including the effect of the interparticle cohesion forces I_p. Different numerical expressions for A were established by fitting semi-empirical relations to these experimental data, each of them corresponding to a different range of the friction Reynolds number R_{*t}.

[12] These semi-empirical expressions provide a satisfying estimation of the threshold friction velocity on a smooth surface u^{ts}_{drag} as a function of the particle diameter D_p for a range of atmospheric density ρ and dust particle density ρ_d. The Martian atmospheric dust presumably is related to the surface dust and soils, representing the finest grained materials produced from mechanical and/or chemical weathering of surface deposits. Earth' and Mars' atmospheric dust particles appear to share similar mineral compositions [see, e.g., *Hamilton et al.*, 2005, Table 3]. Therefore, we reasonably assumed their densities to be similar and we adopted in the following calculations $\rho_d = 2.65$ kg.m^{-3}.

2.3. Parameterization of the Drag Partition

[13] A second factor that strongly affects the erosion threshold in natural situations is the presence of nonerodible elements (gravel, stones, pebbles, boulders). They affect the erosion threshold in two ways. First, the roughness elements cover part of the surface and thus protect it from the aeolian erosion. Secondly, they consume part of the wind momentum that will not be available to initiate particle motion. This leads to a global decrease of the wind shear stress acting on the erodible surface and thus of the erosion efficiency. A physical scheme of the drag partition between the roughness elements and the erodible surface is therefore necessary to parameterize the "effective" threshold friction velocity u^{t}_{drag} over "rough" surfaces.

[14] For practical and predictive applications, *Raupach* [1992] initially proposed an analytical expression of the drag partition on a rough surface based on a dimensional analysis and some physically based assumptions. The proposed equation gives the ratio of the overall wind shear stress τ to the wind shear stress on the smooth, uncovered surface τ_s as a function of the roughness density λ (see section 3.1.1), the ratio σ of the roughness elements' basal to frontal area, the ratio $\beta = \frac{C_R}{C_S}$ of the drag coefficients of an individual roughness element and of the smooth surface, and an empirical parameter m:

$$\frac{\tau}{\tau_s} = \frac{1}{1 - m\sigma\lambda}\,\frac{1}{1 + m\beta\lambda} \tag{5}$$

Though agreeing well with measurements performed in wind-tunnel experiments and on natural sites, this expression was however found to be quite inappropriate for large-scale modeling issues. Its adjustment to measured ground-truth erosion data has led to the recommendation of two kinds of values for m according to the stabilization state of the particle bed [*Raupach et al.*, 1993]; but no objective method to generalize these values for large-scaled modeling were indicated and this empirical parameter does not seem to refer to and/or correlate with any measurable physical value. *Gillies et al.* [2010] recently explored the effect that large roughness elements may have on the entrainment of sediment by Martian winds using a shear stress partitioning approach based on Raupach et al. model. They concluded that developing global or regional dust transport models using such an expression would be a very complex exercise.

[15] An alternative specification of the drag partition was therefore developed by using the aerodynamic roughness length, which appeared to be a more integrative parameter to represent the loss of wind momentum attributable to the roughness elements. The physical basis of that approach was proposed by *Arya* [1975] to determine the wind stress on the Arctic pack ice. As introduced previously, the wind profile in the Surface Boundary-Layer is assumed to be logarithmic in neutral conditions [*Priestley*, 1959] and defines both the overall friction velocity u_{drag} and the global aerodynamic roughness length z_0. *Arya* [1975] assumed that an Interactive Boundary-Layer (IBL) develops between the roughness elements as well. On small enough scales within this IBL, there are effectively no roughness elements. Defined within this IBL, which is also characterized by a logarithmic profile, there is therefore as well a small-scale friction velocity u^{s}_{drag} and a local aerodynamic roughness length corresponding to the intervening erodible surface, i.e. an aerodynamic roughness length on a smooth surface z_{0s}. By connecting the two profiles at the top of the IBL, the ratio of the small-scale friction velocity u^{s}_{drag} to the overall friction velocity u_{drag} can be determined as a function of both the aerodynamic roughness length z_0 and the aerodynamic roughness length z_{0s} of the erodible part of the surface, i.e. the smooth surface existing between the roughness elements. For convenience, an effective friction velocity ratio f_{eff} is defined as the ratio of small-scale to overall friction velocities:

$$f_{eff}(z_0, z_{0s}) = \frac{u^{s}_{drag}}{u_{drag}} = 1 - \frac{\ln\left(\frac{z_0}{z_{0s}}\right)}{\ln\left(0.35\left(\frac{10}{z_{0s}}\right)^{0.8}\right)} \tag{6}$$

where z_0 and z_{0s} have units of centimeters.

[16] This partition scheme has been validated by comparison with shear stress partition measurements performed in wind-tunnels for a large range of values for both the global aerodynamic roughness length z_0 [*Marshall*, 1971] and the aerodynamic roughness length on a smooth surface z_{0s} [*Alfaro and Gomes*, 1995]. Combining the relation between the threshold wind friction velocity on a smooth surface u^{ts}_{drag} and the particle diameter D_p (equation (3)) with this partition scheme provides a parameterization of the threshold

wind friction velocity u^t_{drag} for any surface submitted to erosion:

$$u^t_{drag}(D_p, z_0, z_{0s}) = \frac{u^{ts}_{drag}(D_p)}{f_{eff}(z_0, z_{0s})} \quad (7)$$

This parameterization of the threshold wind friction velocity u^t_{drag} has been successfully used for terrestrial applications, to quantify the fraction of the total wind shear stress acting on the erodible surface to mobilize the soil-derived dust particles [*Marticorena and Bergametti*, 1995]. It has been tested by comparison with wind-tunnel measurements [*Gillette et al.*, 1982; *Nickling and Gillies*, 1989] and field measurements made on various natural sites in semi-arid regions, ranging from smooth erodible surfaces to surfaces totally protected from erosion [*Marticorena and Bergametti*, 1995; *Marticorena et al.*, 1997]. *King et al.* [2005] showed that *Raupach et al.*'s [1993] model predictions were better than *Marticorena and Bergametti*'s [1995] model owing to the incorporation of more variations in the roughness geometry and the alterations to the flow they can cause. However, *Raupach et al.*'s [1993] model requires more inputs and is therefore quite difficult to apply for large-scaled modeling.

[17] Classically, the aerodynamic roughness length z_{0s} of an erodible smooth surface is estimated as a function of the size of the erodible particles. A relation between the size of the particles composing a quiescent sand bed and its aerodynamic roughness length is generally admitted to be [*Bagnold*, 1941; *Greeley and Iversen*, 1985]:

$$z_{0s} = \frac{D_p}{30} \quad (8)$$

For the typical size range of the erodible particles (10 to 2000 μm) this relation leads to values for the aerodynamic roughness length on a smooth surface z_{0s} of the order of 10^{-4} to 10^{-3} cm. Such values have been measured in wind-tunnels [*Gillette et al.*, 1982; *Li and Martz*, 1994] for smooth surface. According to relation 8, the aerodynamic roughness length on a smooth surface z_{0s} is expected to vary from one soi1 to another in relation to their particle size distribution. It is therefore important to test the sensitivity of the partition scheme to this parameter and the precision required for its determination. When using a mean value of $\sim 10^{-3}$ cm to represent the whole range of values for the aerodynamic roughness length on a smooth surface z_{0s}, the errors on the computation of the effective friction velocity ratio f_{eff} are lower than 20% for the major part of the usual range of values for the global aerodynamic roughness length z_0 and exceed 40% only for the very low values [*Marticorena and Bergametti*, 1995]. Thus a value of the aerodynamic roughness length on a smooth surface $z_{0s} = 10^{-3}$ cm can be generally considered as a correct estimation for most of the natural conditions, for which the aerodynamic roughness length on a smooth surface z_{0s} will be controlled by the size of the erodible particles. Assuming that these physics principles which describe the shear stress partitioning can be applied to the Martian surface boundary layer, this parameterization of the threshold wind friction velocity on any surface u^t_{drag} can be used to estimate the erosion thresholds on Mars as a function of its roughness. This requires beforehand the knowledge of the surface pressure P and temperature T - in order to calculate the density ρ at the surface -, the soil size distribution D_p and the aerodynamic roughness length z_0.

[18] Until recently, there have not been enough surface data available to estimate a spatially variable threshold wind friction velocity u^t_{drag} (or a related spatially variable wind shear stress threshold τ^t) accounting for the effects of surface roughness elements on the drag partition scheme nor, for that matter, to derive a map for the physical factors that are controlling it (soil size distribution D_p, aerodynamic roughness length z_0). As we showed previously, the aerodynamic roughness length especially affects the model-calculated wind stresses and wind stress thresholds for dust lifting; a spatially varying aerodynamic roughness length field could thus affect the whole simulated dust cycle. Until now, most of MGCM simulations have thus assumed a spatially uniform aerodynamic roughness length within the 0.1–1 cm range estimated for the Viking landing sites [*Sutton et al.*, 1978], while the aerodynamic roughness length is expected to vary spatially by 3 or 4 orders of magnitude as it is the case in terrestrial arid areas and should be the case in their Martian counterparts.

3. Methodology for Mapping the Aerodynamic Roughness Length

[19] Apart from direct in situ experimental measurements of some dynamical parameters (wind velocity, air temperature and humidity), the only way to determine the aerodynamic roughness length z_0 of any rough surface is to study its correlation with the surface roughness; a key parameter for surface-atmosphere exchanges of mass and energy. The surface roughness can usually be estimated through the use of different techniques depending on the data availability and accessibility in a given region which can therefore produce retrievals at different scales. Once the surface roughness has been retrieved, it can be formally translated to an aerodynamic roughness length through the practical application of different empirically derived correlated relationships based on ground-truth in situ measurements.

3.1. Geometric Roughness and Aerodynamic Roughness

[20] The common approach used to estimate the geometric surface roughness of an erodible surface is based on the close inspection of some geomorphologic features [*Callot et al.*, 2000] and/or some characteristics of the surface roughness elements [*Lettau*, 1969; *Raupach*, 1992; *Lancaster and Baas*, 1998; *Lancaster*, 2004; *Marticorena et al.*, 1997, 2006] Such features/characteristics may include the granulometry of the loose soil, the geometric dimensions of the rough mineral elements present on the surface like rocks, gravel, pebbles, etc., but also the horizontal and vertical extent of the biological part of the surface, especially vegetation.

3.1.1. Determination of the Roughness Density λ

[21] Among the different parameters characterizing the geometrical surface roughness, the roughness density λ, also called the lateral cover L_c, is commonly used as a measure of the roughness characteristics [see, e.g., *Marshall*, 1971].

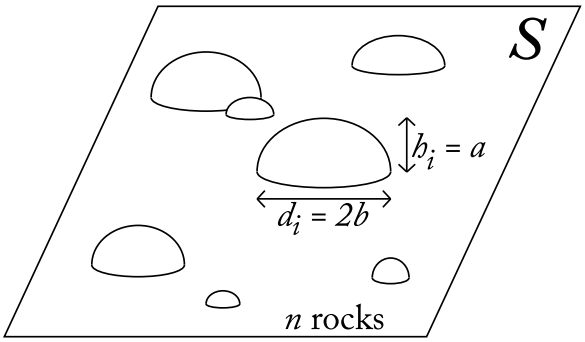

Figure 1. Geometric dimensions of our Martian semi-ellipsoidal-shaped roughness elements.

The interaction between the wind shear stress and the surface roughness is dependent on the vertical surface of obstacles exposed to the wind. The roughness density λ is thus defined as the sum of the frontal silhouette areas f_i of each obstacle present on the surface and facing the wind direction divided by the surface footprint area S:

$$\lambda = \frac{nf}{S} = \sum_{i=1}^{i=n} \frac{f_i}{S} \tag{9}$$

where n and f are, respectively, the number and the arithmetic mean frontal silhouette area of the obstacles present over this given horizontal surface area S and facing the wind direction. The mean frontal silhouette area f can be computed from the geometrical dimensions of the obstacles, given the shape of the obstacles. On the basis of this definition, the roughness density λ can be estimated by counting the obstacles present on a representative surface of any rock abundance ζ and by measuring their geometrical dimensions. Preliminary assumptions on the roughness element shapes are therefore mandatory to allow a determination of the roughness density λ from the geometrical dimensions of the roughness elements.

[22] From direct observations and photographs of the different types of obstacles, we adopted a semi-ellipsoidal shape for our Martian and Martian-analog roughness elements: gravels, pebbles and boulders. The area S of a semi-ellipse is given by: $S = \pi ab/2$, a being the short axis and b the long axis of the ellipse. This equation can be applied to any roughness elements i of diameter d_i and height h_i with $d_i = 2b$ and $h_i = a$ (see Figure 1).

[23] The surface area covered by each roughness element i is thus given by:

$$s_i = \frac{\pi d_i^2}{4} \tag{10}$$

while its frontal surface is given by:

$$f_i = \frac{\pi h_i d_i}{4} \tag{11}$$

Applying these relations to an entire field of study of total surface area S, allows to link the total rock abundance ζ, the total roughness density λ and the geometric dimensions of the n roughness elements present on the field.

$$\zeta = \sum_{i=1}^{i=n} \frac{s_i}{S} = \sum_{i=1}^{i=n} \frac{\pi d_i^2}{4S} = \frac{n\pi D_m^2}{4S} \tag{12}$$

$$\lambda = \sum_{i=1}^{i=n} \frac{f_i}{S} = \sum_{i=1}^{i=n} \frac{\pi h_i d_i}{4S} = \frac{n\pi H_m D_m}{4S} \tag{13}$$

where H_m and D_m are the generalized means associated with the height and diameter, respectively, of the total number of rocks in this rock population.

3.1.2. Relation Between the Roughness Density λ and the Aerodynamic Roughness Length z_0

[24] To estimate the aerodynamic roughness length for terrestrial arid areas from the geometric dimensions of the roughness elements, *Marticorena et al.* [1997] established an empirical relationship between the roughness density λ and the ratio of aerodynamic roughness length to the mean height of the roughness elements z_0/H_m. This relationship, given by equations (14) and (15) and illustrated in Figure 2, was mainly derived from wind-tunnel experiments using artificial roughness elements but also included some data obtained over vegetated surfaces in semiarid areas [*Marshall*, 1971; *Jarvis et al.*, 1976; *Garratt*, 1977; *Raupach et al.*, 1980; *Musick and Gillette*, 1990; *Raupach*, 1991]. The numerical relationship used throughout this paper has been corrected for a calculation error in the original *Marticorena et al.* [1997] paper, as detailed by *King et al.* [2005]. The credibility of the corrected relationship was confirmed by the experimental wind-tunnel data [*Minvielle et al.*, 2003; *King et al.*, 2005] and has been found to be valid when applied to natural desert surfaces [*Marticorena et al.*, 2006].

$$\text{For } \lambda < 0.0408 \ \log_{10}\left(\frac{z_0}{H_m}\right) = 1.31 \times \log_{10}(\lambda) + 0.66 \tag{14}$$

$$\text{For } \lambda \geq 0.0408 \ \log_{10}\left(\frac{z_0}{H_m}\right) = -1.16 \tag{15}$$

[25] In practice, the generalization on a scale compatible with MGCMs of the empirically derived relationship between the geometric and aerodynamic roughnesses given in 14 and 15 is quite limited. Its practical application on a global scale is indeed difficult since it would require (1) an exhaustive and accurate documentation of the geometric roughness on the whole surface of Mars and (2) multiple field observations to precisely calibrate the information on the aerodynamic roughness. However, only very few field measurements of both aerodynamic roughness length and geometrical characteristics of the Martian surface are available.

3.2. Remote Sensing Data and Aerodynamic Roughness

[26] For terrestrial arid and semiarid natural areas, another approach consists in estimating the aerodynamic roughness

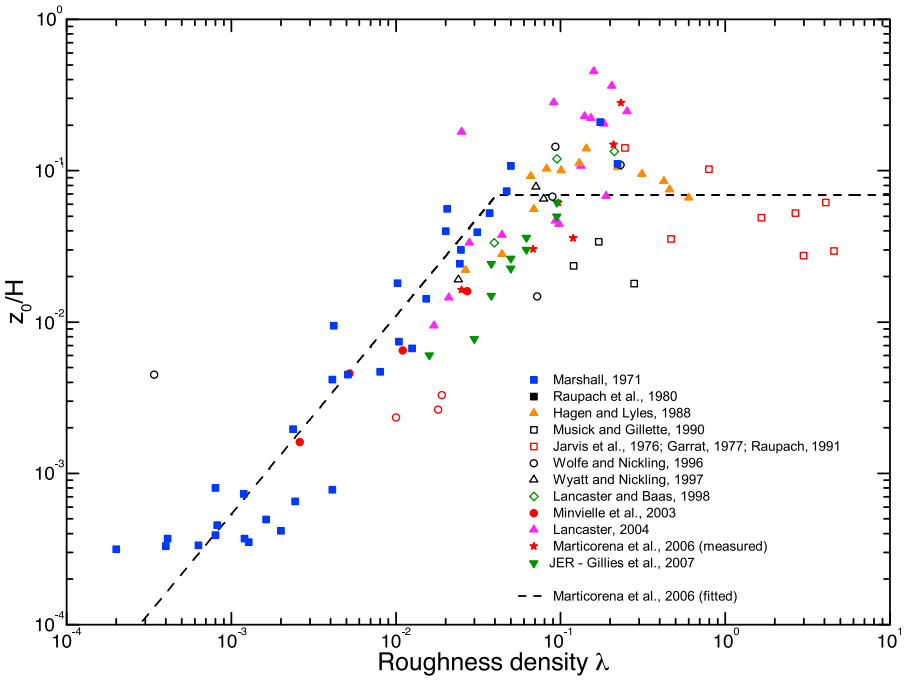

Figure 2. Ratio of the aerodynamic roughness height z_0 to the generalized mean height H_m of the roughness elements as a function of the roughness density λ.

of an erodible surface by using remote sensing data or, more specifically, by mapping the surface geometric roughness at a global scale through the scattering behavior of an incident beam of radiation on a naturally rough surface and calibrating it with the corresponding aerodynamic roughness measured in situ in a number of sites. *Greeley et al.* [1991, 1997] and *Marticorena et al.* [2006] have experimentally correlated the aerodynamic roughness length with C- and L-band radars backscatter cross section σ_0 obtained from both aircraft and/or spacecraft data. These correlations were validated by using ground-truth data derived from wind profile measurements over various arid and semi-arid terrestrial surfaces (Death Valley and Lunar lake, USA; Gobabeb, Namibia; North Africa). Recently, *Marticorena et al.* [2004] and *Laurent et al.* [2005, 2008] have investigated the possibility of retrieving the aerodynamic roughness length of terrestrial arid areas using the bidirectional reflectance distribution function (BRDF) derived from passive multidirectional measurements in the solar spectrum of the Polarization and Directionality of the Earth Reflectance (POLDER-1) radiometer. They established an empirical relationship between the aerodynamic roughness length and the so-called protrusion coefficient (PC) of the surface derived from the POLDER-1 bidirectional reflectance distribution function (BRDF) and applied it successfully over the Sahara, the Arabian Peninsula and the eastern Asian deserts. These latest remote sensing approaches appear to be a valuable alternative to the in situ measurement techniques for generalizing these empirical estimations to remote areas with severe climatic conditions such as dry hot deserts.

[27] The application to Mars of these most valuable remote sensing techniques currently used on Earth appears quite limited by the fact that no C- nor L-band radars currently orbit, have orbited, or have ever been fully proposed to orbit around this planet. Following *Menenti and Ritchie* [1994] and *De Vries et al.* [2003] and their use of high-resolution airborne laser altimetry to determine roughness element properties in complex vegetated areas, *Heavens et al.* [2008] succeeded in deriving two different aerodynamic roughness length z_0 maps representing a plausible range for Mars under typical conditions by using high-resolution laser altimetry data from the Mars Orbiter Laser Altimeter (MOLA) onboard Mars Global Surveyor (MGS). Their first aerodynamic roughness length map was scaled directly from the surface geometric roughness derived from the MOLA topography (as a composite of 0.6, 2.4, and 9.2 km baseline lengths [*Kreslavsky and Head*, 2000]), by assuming that centimeter-to-kilometer-scaled roughness on Mars follows overall fractal self-affine statistics and by calibrating it further with the results from the Mars PathFinder wind measurements [*Sullivan et al.*, 2000]. Their second aerodynamic roughness length map was derived from the MOLA beam scattering, presumed to provide a measure of a relative surface geometric roughness on the footprint-scale of the optical pulse width (~75 m) [*Neumann et al.*, 2003] that was further calibrated with the uniform aerodynamic roughness length z_0 = 16.62 cm used in the Geophysical Fluid Dynamics Laboratory Mars GCM [*Wilson and Hamilton*, 1996].

3.2.1. Rock Abundance on Mars

[28] Other data sets have however emerged in the past years that also enable the mapping of the surface geometric roughness at a global scale, as required for the estimation of mineral dust emissions on Mars. Indeed, nighttime infrared spectral observations returned from Martian orbiters can been used for determining the spatial distribution of rocks at the surface of Mars. The thermal inertia of any material represents its ability to conduct and store heat. In the context of planetary

sciences, it is a measure of a (sub)surface's ability to store heat during the day and radiate it during the night. Thermal inertia I is defined as $I \equiv \sqrt{k\rho C}$ where k is the bulk thermal conductivity, ρ the bulk density and C the specific heat capacity of the surface. For a surface such as that of Mars, it predominantly depends on the physical properties of the surface materials such as particle size, degree of induration (i.e., cementation of grains), rock abundance, and exposure of bedrock within the top few centimeters of the subsurface. In general, surfaces of unconsolidated, fine-grained materials will have low values of thermal inertia, whereas cemented surfaces and surfaces composed of sand-sized grains will have intermediate values, and rocky surfaces and bedrock outcrops will have higher values. By checking the consistency of the thermal inertia signal at high resolution with Viking image mosaics, *Mellon et al.* [2000] observed correlations between the spatial variations in thermal inertia and local geomorphological features, suggesting some relationship between the centimeter-scale surface layer in these thermally mapped regions and the tens to hundreds of meter-scale morphology. Whereas daytime thermal observations are dominated by the topography, the atmospheric emissivity, the global albedo and surface emissivity, which are in turn controlled by the mineralogic composition of concerned materials, the nighttime thermal emission is primarily controlled by the surface thermophysical properties. Since a surface made of materials with different brightness temperatures does not behave as a homogeneous blackbody, nighttime multiwavelength observations can be inverted to split up the thermal contributions of the different components and to retrieve the fraction of the surface covered by each of them. Using such a thermal differencing technique on the measurements of the InfraRed Thermal Mapper (IRTM) onboard Viking and the Thermal Emission Spectrometer (TES) onboard Mars Global Surveyor (MGS), *Christensen* [1986] and *Nowicki and Christensen* [2007] provided estimates of rock abundance ζ with spatial resolutions of $1^\circ \times 1^\circ$ and $1/8^\circ \times 1/8^\circ$, respectively. Their results indicate a total abundance or surface area of rocks greater than 10–15 cm diameter versus fine component materials such as soil, dust or sand [*Christensen*, 1982] and are believed to be accurate up to about 20% [*Christensen*, 1986; *Nowicki and Christensen*, 2007]. A direct intercomparison between these two different data sets proved to be difficult considering their differences in spatial resolution and sampling of observations. Their agreement is nonetheless quite satisfactory. Both reveal the same overall morphological features and their relative rock distributions match on the global scale. *Nowicki and Christensen* [2007] have claimed that the use of the high resolution MGS-TES data is likely to survey surfaces possibly resulting from a single or uniform set of geologic processes such as impact cratering, fluvial erosion, volcanic flows and/or, what particularly appeals us here, aeolian erosion. MGS-TES data seem therefore particularly suitable to serve our calculations of the aerodynamic roughness length. However, the estimation of the rock abundance ζ from MGS-TES observations is currently restricted between latitudes 60°S and 60°N. It is therefore mandatory to extend the range of MGS-TES rock abundance data set to these areas, well beyond the current limited coverage, before using the computed maps in a MGCM (see section 4).

3.2.2. Relation Between the Rock Abundance ζ and the Aerodynamic Roughness Length z_0

[29] By assuming a semi-ellipsoidal shape for the roughness elements, equations (12) and (13) give:

$$\lambda = \frac{H_m}{D_m} \times \zeta. \tag{16}$$

[30] Knowing the rock abundance ζ, it is thus possible to introduce it into equations (14) and (15) to infer the associated aerodynamic roughness length :

$$\text{For } \zeta < 0.0408 \times \frac{D_m}{H_m} \quad \log_{10}\left(\frac{z_0}{H_m}\right) = 1.31 \times \log_{10}\left(\frac{H_m}{D_m} \times \zeta\right) + 0.66 \tag{17}$$

$$\text{For } \zeta \geq 0.0408 \times \frac{D_m}{H_m} \qquad \log_{10}\left(\frac{z_0}{H_m}\right) = -1.16 \tag{18}$$

[31] If the knowledge of the rock abundance ζ appears essential to estimate the aerodynamic roughness length, it is far from being sufficient since it depends also on some rock size parameters, namely the mean height H_m and mean diameter $D_m$of the specific rock population (see section 5).

4. Extension of the MGS-TES Rock Abundance Global Map

[32] Because of cold temperatures, icy seasonal surfaces and high solar incidence angle at high latitudes, neither MGS-TES nor Viking-IRTM rock abundance data sets extend poleward of 60° latitude. Moreover, rock abundances for surfaces that have extremely low nighttime surface temperatures or high dust opacities (e.g. Olympus Mons, Hellas basin), which prevent good systematic data coverage, are also unknown [*Nowicki and Christensen*, 2007]. The spectral difference algorithm used by *Nowicki and Christensen* [2007] from nighttime thermal infrared observations to determine the rock abundance on the surface of Mars provided correlated information between thermophysical properties, global albedo and local morphologies. Those properties proved to be useful to characterize the Martian surface and to interpret the nature of the materials present. Thus, with the aim of filling both the [60°N, 90°N] and [60°S, 90°S] region, we have made the assumption that the rock abundance of a given area could be well constrained by both its thermal inertia I and its albedo α. For more consistency, we have used the latest version of thermal inertia [*Putzig and Mellon*, 2007] and albedo [*Christensen et al.*, 2001] global maps derived from the Thermal Emission Spectrometer (TES) aboard Mars Global Surveyor (MGS), which both range between latitudes 87°N and 87°S.

4.1. Learning From the [60°S:60°N] Region of Mars

[33] In the [60°S:60°N] MGS-TES data sets with a $1/8^\circ \times 1/8^\circ$ spatial resolution, the thermal inertia and the albedo both range between 0 and 5000 $J.m^{-2}.K^{-1}.s^{-1/2}$ and 0.06–0.32, respectively, with the majority of the points below 1000 $J.m^{-2}.K^{-1}.s^{-1/2}$. We have constructed 2D-bins of thermal inertia and albedo $[I_k, \alpha_l] = [I_k \pm \Delta I/2, \alpha_l \pm \Delta\alpha/2]$ with $\Delta I = 8$ and $\Delta\alpha = 0.006$. Figure 3 is a map depicting the density of grid points on both the MGS-TES thermal inertia I

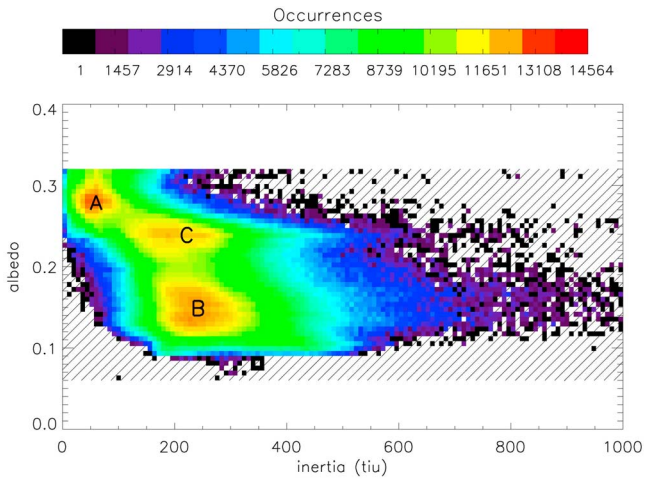

Figure 3. Density of points throughout the different MGS-TES [I_k, α_l] bins. The A, B, and C units are indicated, as defined by *Mellon et al.* [2000]. The grey area corresponds to empty bins. For convenience, the map was limited to thermal inertia I values ≤1000 J.m^{-2}.K^{-1}.s$^{-1/2}$.

and albedo α global maps whose values belong to a certain 2D-bin. In other words, the plot shows for each [I_k, α_l] bin, the number of 1/8° × 1/8° pixels of both the MGS-TES thermal inertia and albedo global maps having simultaneously a thermal inertia value enclosed between $\Delta I_k - \Delta I/2$ and $I_k + \Delta I/2$, and an albedo value enclosed between $\alpha_l - \Delta\alpha/2$ and $\alpha_l + \Delta\alpha/2$. Empty bins mean that no pixel in the MGS-TES global maps was found within the corresponding range of thermal inertia I and albedo α.

[34] Figure 3 clearly displays three modes for the density, (low I, high α), (high I, low α) and (intermediate to high I, intermediate α), as already pointed out by *Mellon et al.* [2000] who defined accordingly A, B and C soil types, respectively (see Table IV of their study). Each non-empty [I_k, α_l] bin points to a corresponding rock abundance distribution (hereafter : bin-distribution) extracted from the corresponding pixels of the MGS-TES rock abundance global map. It might be a single point (if there is only one pixel in the bin) or a well-defined distribution. The observed MGS-TES bin-distributions might be either very scattered or clearly defined with a peak value. Some MGS-TES bin-distributions are even bimodal, i.e. with two values of rock abundance corresponding to an absolute and a local maximum in the bin-distribution. Figure 4 gives an overview of

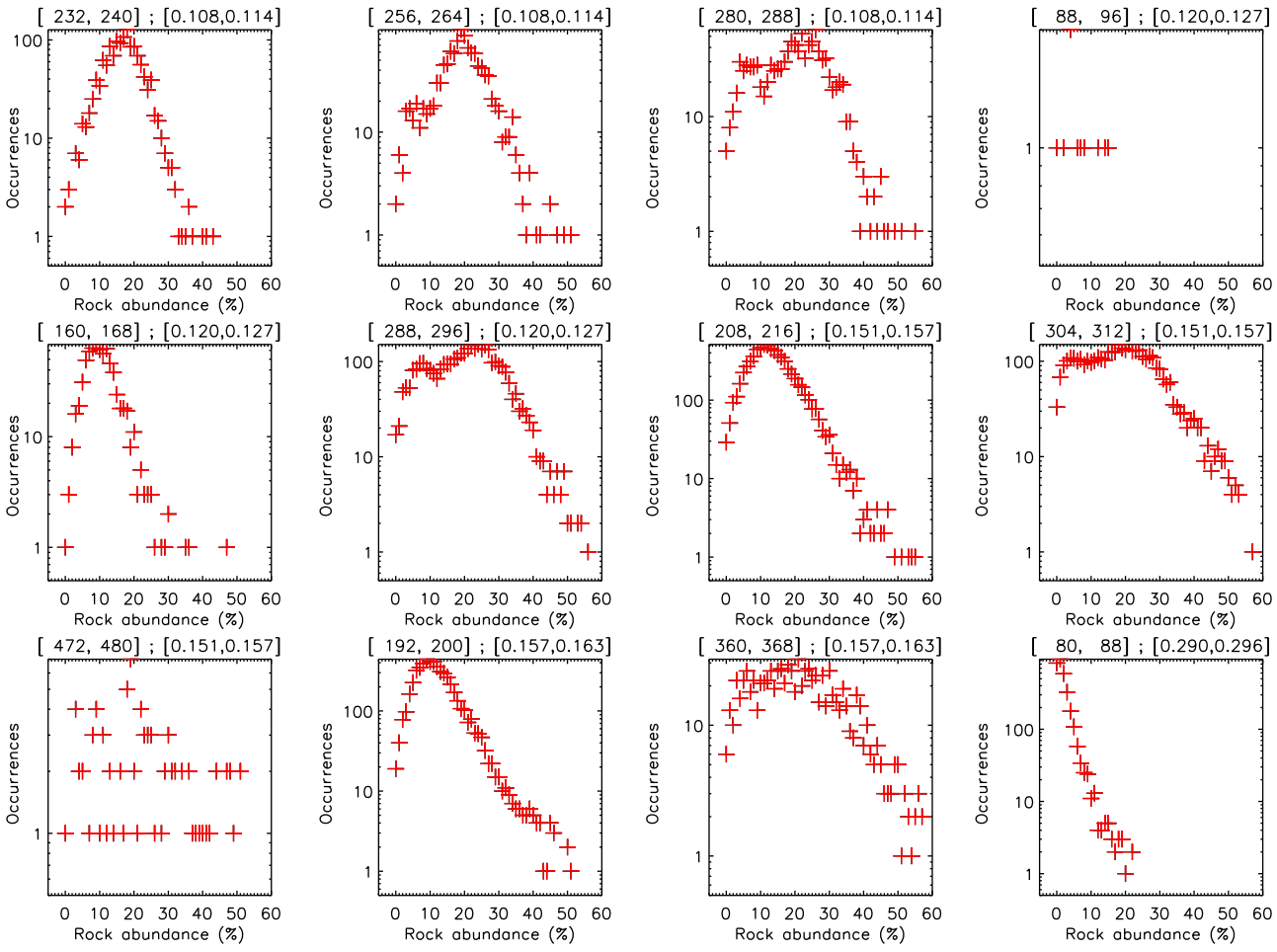

Figure 4. Example of MGS-TES rock abundance distributions (bin-distributions) found in different MGS-TES [I_k, α_l] 2D-bins and plotted on a log-scale. The numbers displayed above each graph represent the studied ranges of thermal inertia I and albedo α, [$I_{k_{min}}$, $I_{k_{max}}$] and [$\alpha_{l_{min}}$, $\alpha_{l_{max}}$], respectively.

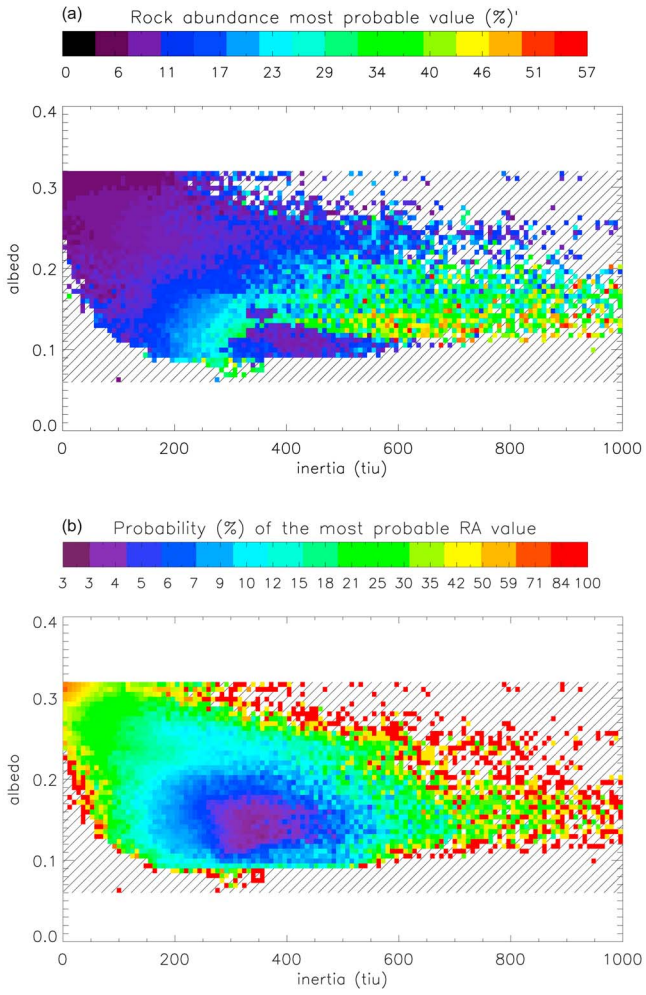

Figure 5. Most probable values of the MGS-TES rock abundance bin-distributions and associated probability.

some statistical MGS-TES bin-distributions. In order to extrapolate the MGS-TES rock abundance global map poleward, we have attempted to choose the most representative rock abundance value for each [I_k, α_l] 2D-bins. To do so, we have extracted from each bin-distribution the mode value, or most probable value, (i.e the value with the largest occurrence in the considered bin-distribution) rather than the mean or the median value. The most probable value exhibits the higher probability of occurrence over the whole set of MGS-TES bin-distributions. It is therefore the most likely parameter to be a relevant proxy for the rock abundance of a soil characterized by [I_k, α_l] 2D-bin distributions.

[35] Figure 5 is constructed in the same manner as Figure 3 except that the color scale is correlated to the most probable rock abundance value of each MGS-TES bin-distribution and its associated probability of occurrence in each [I_k, α_l] bin. It appears that the three modes observed in the density map displayed in Figure 3 are not represented anymore in Figure 5. The A, B, C units all correspond to representative values of rock abundance lower than 15%, with some values of rock abundance higher than 15% found only in the B unit. However, the pattern suggests a global trend : from the left top corner of the map (high albedo - low inertia), the rock abundance value increases toward the right bottom corner (mid-to-low albedo - high inertia) with an exceptions for bins around I = 400 J.m^{-2}.K^{-1}.s$^{-1/2}$ and α = 0.1 that alter this global trend with an isolated pocket of low rock abundance values, however well restrained to a small area. The overall appearance thus remains a well established pattern. Thermal inertia and albedo by themselves do not provide a unique characterization of the surface physical characteristics [*Christensen*, 1982], but do provide significant insight into the physical nature of the surface [*Fergason et al.*, 2006]. The shape and color of the scatterplot indicate indeed that a most probable value of the rock abundance can be inferred for each bin-distribution from the combined consideration of both its thermal inertia I_k and its albedo α_l. This pattern we uncovered legitimates the use of both the thermal inertia and albedo for characterizing a most probable rock abundance value. The information contained in this map has been used to extend the rock abundance map poleward to latitudes higher than 60°S and 60°N.

4.2. A Closer Look to the Limited North [50°N:60°N] and South [60°S:50°S] Bands

[36] Before extrapolating the rock abundance, we have investigated the closest region to each pole in order to determine whether any bias could be caused by terrain too far from the regions of interest. Figure 6 displays the density of points throughout the different bins for both the north band [50°N:60°N] and the south band [60°S:50°S] and their associated most probable values. The density patterns observed in both regions are not the same, suggesting different terrains/morphologies close to each pole. Besides, the most probable rock abundance values displayed for the same two regions are different where the same [I_k, α_l] bins overlap. This justifies the need of accounting as much as possible for the different terrains - northern and southern ones - when extrapolating poleward.

[37] Nevertheless, the [I_k, α_l] bins in both these limited bands ([50°N:60°N] and [60°S:50°S]) do not extend to thermal inertia I_k values as high as they do in both polar regions ([60°N:90°N] and [90°S:60°S]). It is therefore mandatory to rely on the entire [60°S:60 °N] reference region to achieve a complete extrapolation, when the information is missing from the north and the south band. Finally, some [I_k, α_l] bins that are represented in the polar regions are missing from the [60°S:60°N] reference region. This limitation is actually due to the high thermal inertia values (above 1000 J.m^{-2}.K^{-1}.s$^{-1/2}$) of the exposed ice at the surface, in both polar regions (Figure 7).

4.3. Extrapolating Poleward

[38] Estimation of the rock abundance values at the poles was performed as follows. For each non-empty [I_k, α_l] bin present in the polar regions, the corresponding rock abundance value was extracted from the reference density maps, first by looking at the nearest non-polar band (i.e. [50°N:60°N] or [50°S:60°S] for the [60°N:90°N] or [60°S:90°S] region respectively) and then at the [60°S:60°N] region when the corresponding [I_k, α_l] bin was missing from the nearest non-polar band. The extrapolated rock abundance map obtained is shown in Figure 8. The transition at 60°N remains globally visible. The transition between the south

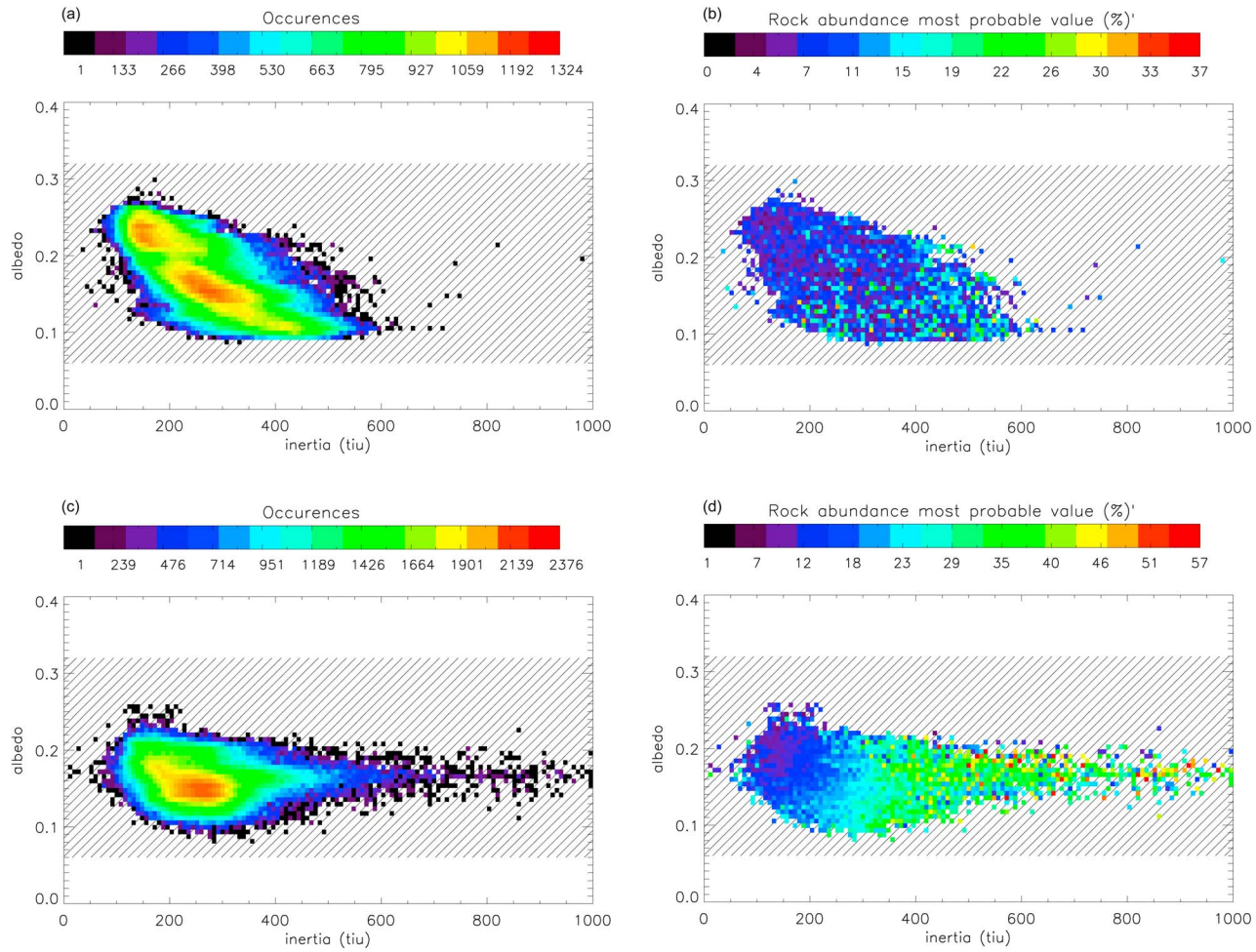

Figure 6. (a, c) Density of points and (b, d) most probable values throughout the [I_k, α_l] bins in the north band [50°N:60°N] (Figures 6a and 6b) and in the south band [60°S:50°S] (Figures 6c and 6d).

band and the South polar cap remains somewhat rough mainly at the south of Argyre Planitia whereas it is smoother on the higher terrains (Terra Sirrenum, Aonia Terra, Noachis Terra, Promethei Terra Cimeria).

4.4. Extrapolating in the Tharsis Region and in Hellas Planitia

[39] The initial MGS-TES rock abundance global map displays missing values not only poleward of 60°N and 60°S but in the Hellas impact basin and in the Tharsis region as well [*Nowicki and Christensen*, 2007]. These pixels were filled following the same extrapolation technique used for the polar regions.

[40] The Hellas basin displays a very localized and compact region of missing rock abundance values. Most of these were filled by extrapolating rock abundances based on [I_k, α_l] bin values of a region extending between longitudes 20°E and 100°E and between latitudes 20°S and 60°S and thus centered on the Hellas basin. By doing so, the geomorphology of the surrounding region was taken into account as much as possible. However, very few pixels remained unfilled due to a lack of necessary [I_k, α_l] bin values in this region. In order to achieve the extrapolation of the rock abundances in the Hellas basin, the corresponding rock

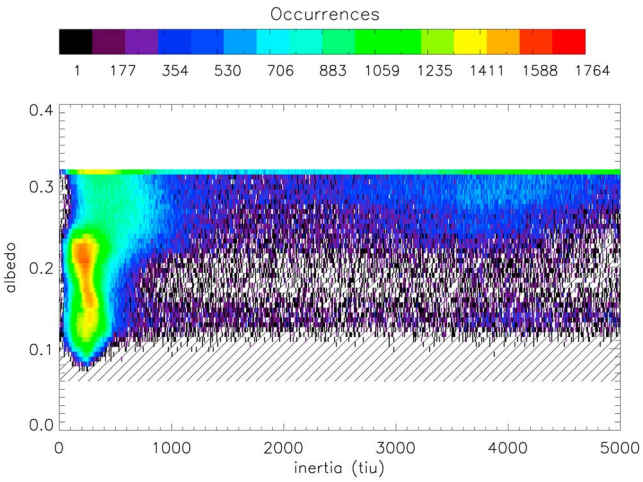

Figure 7. Density of points throughout the [I_k, α_l] bins in the north pole [60°N:90°N]. Many more thermal inertia I values greater than 1000 $J.m^{-2}.K^{-1}.s^{-1/2}$ are involved in the different bins than in the central region, due to exposed ice regions.

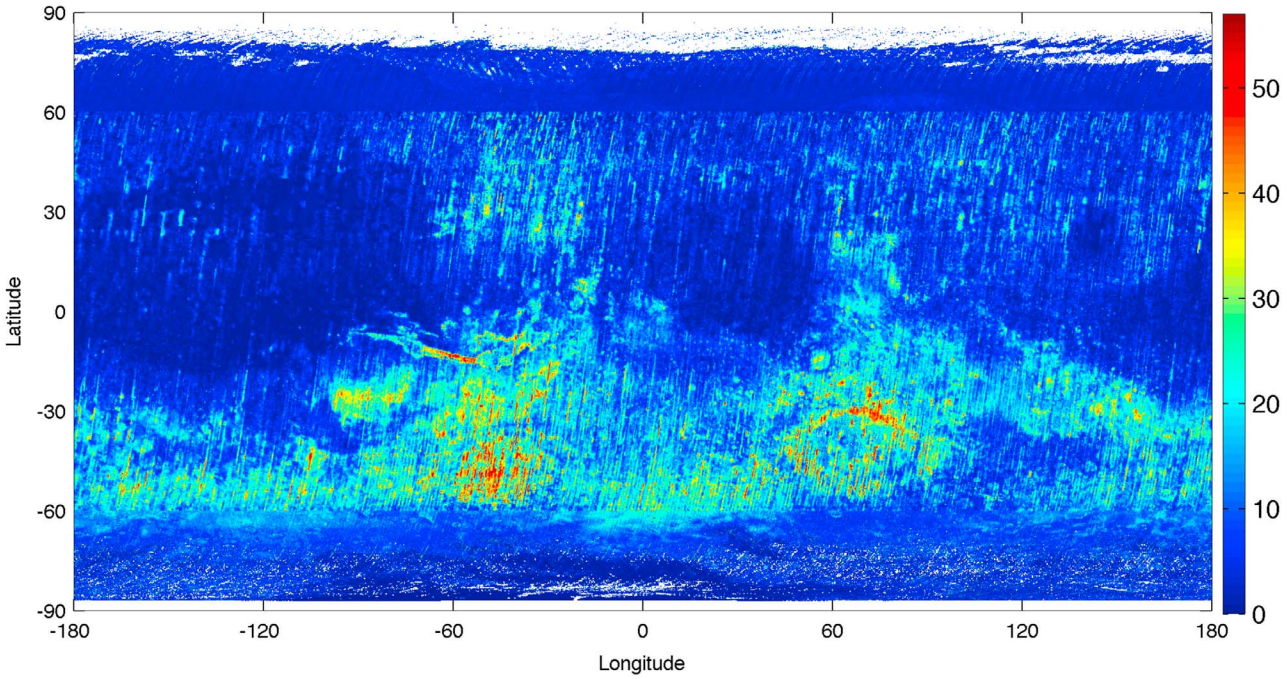

Figure 8. Extended MGS-TES rock abundance data (in %) with a 1/8° × 1/8°spatial resolution. White areas map pixels for which no values could be derived with our method because of missing inertia and albedo data (poleward of 87°) or because of missing references for [I_k, α_l] bins that correspond mainly to areas of exposed ice.

abundance values were extracted from the reference density map of the whole central region [60°N, 60°S].

[41] The missing rock abundance values in the Tharsis region are spread over a wider area. Using directly the corresponding rock abundance values extracted from the reference density map of the whole central region gave a very consistent extrapolation, with respect to the rock abundance values found in the surrounding areas (the whole Tharsis region and heading east from Tharsis, Arabia Planitia).

4.5. Error Analysis on Rock Abundance Data

[42] It is mandatory to estimate the statistical significance related to our extrapolation method using the most probable rock abundance value. Figure 5 displays the actual probability of obtaining the most probable value in each [I_k, α_l] bin. Here again a pattern appears showing that the lowest probabilities - given the reference region [60°S:60°N] - are centered around the (intermediate I, low α) values. The average probabilities to find the most probable values of the rock abundance differ in each of the three modes defined by *Mellon et al.* [2000]. The highest confidence level is to be found in the A mode (above 30%) whereas the lowest confidence level lies in the B mode (below 8%). The C mode provides 10% to 30% probability of displaying the most probable rock abundance value. The low probability in the B mode are partly explained by the presence of a large number of bimodal distributions in the corresponding [I, α] bins. Around these modes and toward the end of the investigated domain, the probability increases: it is due to the diminution of the density in each [I_k, α_l] bin which in return increases the probability of the most probable rock abundance value.

[43] In addition, we ran some sensitivity tests to estimate how the errors attached specifically to the thermal inertia and albedo might influence our grid of [I_k, α_l] bin, their associated bin-distributions and their most probable rock abundance value. Uncertainty in the visible bolometer measurement [*Christensen et al.*, 2001] results in an albedo overall uncertainty of approximately $\Delta\alpha = \pm\ 0.001$ (0.5% relative error for an albedo of 0.2). *Putzig and Mellon* [2007] estimated the different sources of uncertainty in their computations of the nighttime bolometric thermal inertia for a 180 K Martian surface. These sources comprise physics not taken into account by the thermal model and inaccuracies in the ancillary data used on which the computations of *Putzig and Mellon* [2007] rely on, especially the albedo. This results in an thermal inertia overall uncertainty $\Delta I = \Delta\alpha \times f(I)$ where $f(I)$ can be estimated from Figure 4a in the work of *Putzig and Mellon* [2007]. As a result, the median value of the relative error $\frac{\Delta\zeta}{\zeta}$ we get on the determination of the most probable value of rock abundance in each bin, due to the errors on the albedo and the inertia, through the whole reference map of [60°S:60°N], is 0.004% when choosing $\Delta\alpha = 0.001$ and 0.034% when choosing $\Delta\alpha = -\ 0.001$. A very few bins displayed values above 5% and lower than 17% (0.3% and 0.5% of the total for case $\Delta\alpha = 0.001$ and case $\Delta\alpha = -\ 0.001$ respectively). Therefore, the errors on the albedo and on the thermal inertia are not responsible for an appreciable uncertainty in the extrapolation of the rock abundance regarding the natural dispersion already observed in the [I_k, α_l] bins. This dispersion can be quantified by the probabilities $Pr(\zeta)$ of obtaining the most probable rock abundance value in each [I_k, α_l] bin, or by its corresponding

uncertainty $\Delta\zeta$ that can be roughly estimated at $3\sigma(99\%)$ by inversing $Pr(\zeta) = 1 - \frac{2\Delta\zeta}{\zeta([I_k,\alpha_l])}$.

[44] As a whole, the high uncertainties resulting from our extrapolation method emphasize its limitations. Still, it appears to us, at least on a statistical point of view, that it is the best choice to get relevant proxies for different rock abundances, for different surfaces characterized by [I_k, α_l] 2D-bin distributions, and extrapolate them to the whole surface of Mars.

5. Rock Size-Frequency Distributions

[45] The main difficulty before applying to Mars the empirically derived correlated relationship displayed in equations (17) and (18) is the determination of the generalized mean diameter D_m and the generalized mean height H_m associated to a rock population with a rock abundance ζ. Indeed, the roughness elements present at the surface of Mars may exhibit very different size distributions. Though essential to its determination, the knowledge of the rock abundance ζ is far from being sufficient to estimate the aerodynamic roughness length z_0 since this parameter depends also on the rock size-frequency distribution.

5.1. Rock Size-Frequency Distributions on Mars

[46] Understanding the size-frequency distribution of rocks at potential landing sites from remotely observed data is of prime importance for quantifying the hazards for landing a spacecraft, for evaluating the trafficability of any rovers maneuvering and thus for ensuring the mission success. On the basis of the two Viking landers findings, it was first suggested that a power law could be used to describe the populations of rocks greater than 0.1 m [*Moore and Jakosky*, 1989; *Moore and Keller*, 1990, 1991]. By combining the same surface rock counts at Viking 1 and Viking 2 landing sites with Martian-analog rocky locations on Earth (mostly volcanic and alluvial fan surfaces in Death Valley and the Mojave Desert, California, USA), *Golombek and Rapp* [1997] developed an improved model of the observed size-frequency distributions of rocks on Mars. In this model, based on a simple crushing law related to fracture and fragmentation theory, the size-frequency distributions of rocks are fitted with exponential curves of the form:

$$F_k(D) = k \exp^{-q(k)D} \tag{19}$$

where $F_k(D)$ is the cumulative fractional area covered by rocks with diameter greater than or equal to a given diameter D, k is the total fractional area covered by rocks, and $q(k)$ is an exponential factor - approximated by $q(k) = 1.79 + \frac{0.152}{k}$ - governing how abruptly the area covered by rocks decreases with increasing diameter D [*Golombek and Rapp*, 1997]. Rock abundances derived from Viking-IRTM and MGS-TES data are determined for 10 cm and larger blocks on the surface. At this diameter, the cumulative fractional area versus diameter plots tend to flatten out, approaching their total fractional area of rock coverage at smaller diameters. As a result, *Golombek and Rapp* [1997] were able to use the rock abundance derived from the thermal infrared differencing techniques [*Christensen*, 1986; *Nowicki and Christensen*, 2007] as k and to calculate $q(k)$ for any rock abundance value, thereby allowing them to crudely estimate the size-frequency distribution of rocks at any location on Mars. Even though the Viking-IRTM and MGS-TES rock abundances were estimated at spatial resolutions of $1^\circ \times 1^\circ$ ($\sim$60 km) and $1/8^\circ \times 1/8^\circ$ ($\sim$3 km) respectively [*Christensen*, 1986; *Nowicki and Christensen*, 2007], they have been generally quite successful in reproducing the size-frequency distributions of rocks larger than about 10 cm in diameter observed for all subsequent landing sites at much smaller spatial scales ($\sim$10 m) [*Golombek et al.*, 1999, 2005, 2008]. All landing site selection efforts have relied since then on this model to estimate the probability of encountering a rock of any given size over any landing area for any total rock abundance. Since a critical point for assessing the quality of a landing site is to reproduce correctly the population of the most damaging and hazardous rocks, the attention has been especially focused on the size-distribution of the largest rocks.

[47] For our purpose, we have to proceed in a different way from [*Golombek et al.*, 1999, 2005, 2008]. As explained previously, the aerodynamic roughness length, in terms of aerodynamic interactions, is indeed characterized by the roughness density λ which depends not only on the size of rocks but also on their number. This can often lead to situations for which the roughness density λ is completely defined/dominated by the smallest rocks if their number greatly exceeds that of the larger rocks. However, the results obtained by *Golombek and Rapp* [1997] indicate that neither the power law nor the exponential distributions are able to reproduce correctly the populations of the smallest rocks: the power law distributions strongly overestimate them while the exponential distributions significantly underestimate them (see Figure 10). A distribution function able to reproduce with a comparable quality the various-sized components of the whole population is therefore needed. Moreover, preliminary results indicate that the size-frequency distribution of rocks at the Phoenix landing site seems to deviate from the modeled curves. Such a strong deviation suggests that a simple crushing law based on fracture and fragmentation theory used to derive the exponential distributions does not fully explain the rock populations at every Martian site [*Heet et al.*, 2009].

[48] When looking at the number distribution of rocks versus diameter at Viking Lander 1, Viking Lander 2 and Mars PathFinder landing sites (cf. Figure 9), it is clear that the distribution does not follow a monotonically decreasing function (note the maximum values at diameters in the 2–10 cm range). A classical distribution function used to fit such a frequently encountered pattern for environmental and geophysical parameters - such as aerosol size [*Gomes et al.*, 1990] or soil texture [*Chatenet et al.*, 1996] - is the lognormal distribution. One of the advantages of the lognormal distribution is that the parameters characterizing it (median diameter μ and standard deviation σ) have an implicit physical meaning. In our model, any rock population is fitted with a lognormal distribution of the form:

$$f(D, \mu_N, \sigma_N) = \frac{1}{D\sqrt{2\pi\sigma_N^2}} \exp^{-\frac{(\ln D - \mu)^2}{2\sigma_N^2}} \tag{20}$$

where $f(D, \mu_N, \sigma_N)$ is the lognormal distribution describing the number of rocks of each diameter D associated with a

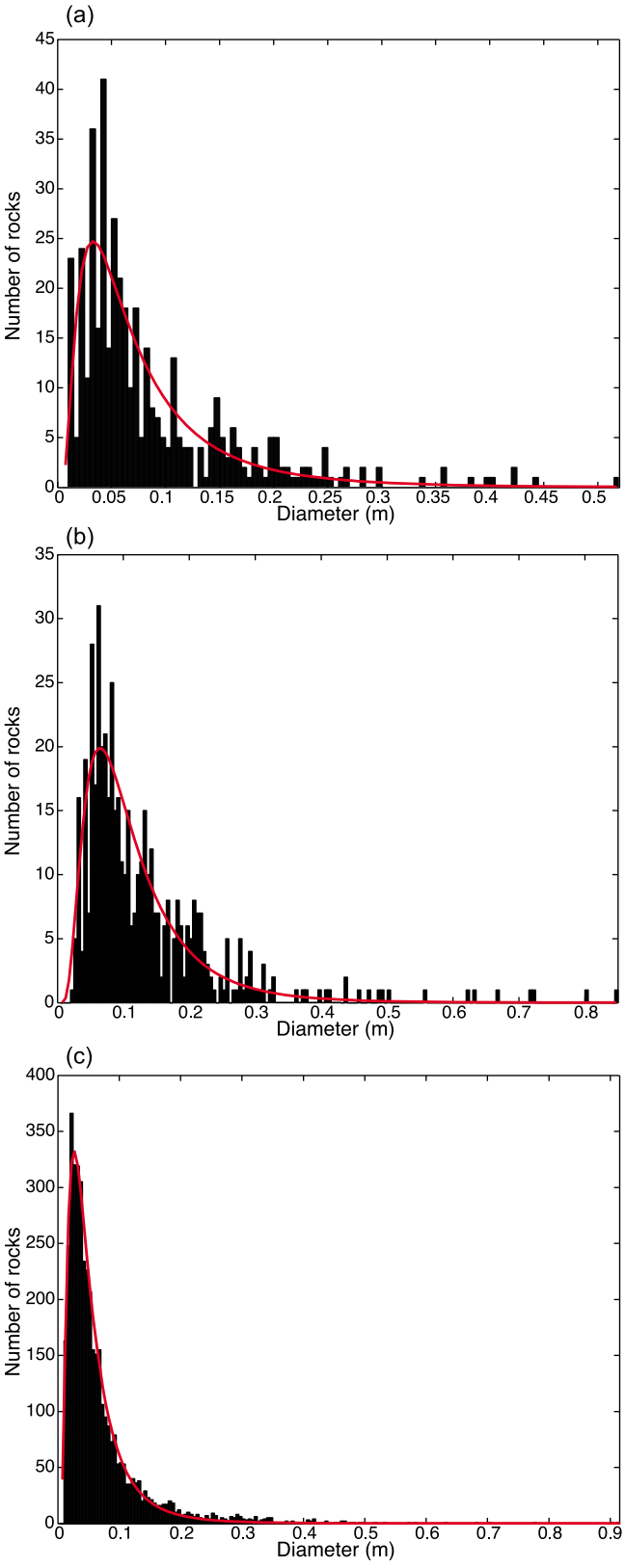

Figure 9. Number distribution of rocks versus diameter at (a) Viking lander 1, (b) Viking lander 2, and (c) Mars PathFinder landing sites (binned to a resolution of a half centimeter) along with our lognormal-modeled distributions for the same sites.

rock population characterized by a median diameter e^{μ_N} and a standard deviation σ_N, in number. There is currently no global knowledge of the size-frequency distributions of rocks on Mars to compare with this model. The only existing direct observations were made around the landing sites where spacecraft have returned data [*Moore and Jakosky*, 1989; *Moore and Keller*, 1990, 1991; *Yingst et al.*, 2007]. We were able to fit the Viking 1, Viking 2 and Mars Pathfinder data with these lognormal distributions. In general, the data on occurrence of various rock diameters at each site may be plotted as histograms showing the number of rocks for each diameter. Accordingly, Figure 9 reports the results of our lognormal least squares fitting procedure on the number distributions of rocks, displayed as the number of rocks of each diameter, at these different landing sites. With Pearson product-moment correlation coefficients $r \geq 0.99$ for all landing sites, our lognormal least squares fitting procedure appears excellent and provides a good and satisfying adjustment for every rock size class. However, in this paper where we are primarily concerned with estimating the relative areal importance of rocks, it is therefore more valuable to deal with the cumulative fractional area covered by rocks of any diameter, integrating from the smallest to the largest rock sizes. In this form, the fractional area of rocks greater than any diameter provides critical and useful information about the surface roughness element populations, and has been widely used in the scientific literature [*Moore et al.*, 1979; *Malin*, 1988; *Golombek and Rapp*, 1997]. We therefore fit our rock populations using a cumulative distribution of the form:

$$F(D,\mu_A,\sigma_A) = \zeta\left(\frac{1}{2} + \mathrm{erf}\left[-\frac{\ln D - \mu_A}{\sigma_A\sqrt{2}}\right]\right) \qquad (21)$$

where $F(D, \mu_A, \sigma_A)$ is the cumulative fractional area covered by rocks greater than any diameter D associated with a rock population characterized by a median diameter e^{μ_A} and a standard deviation σ_A, in fractional area, for a total rock abundance ζ. Figure 10 displays the cumulative fractional area covered by rocks with diameters greater than diameter D versus rock diameter D for the near fields of the Viking 1, Viking 2 and Mars PathFinder landing sites, along with the different theoretical distributions that have been suggested to describe them. As pointed out previously by *Golombek and Rapp* [1997], the power law-modeled distributions suggested by *Moore and Jakosky* [1989] and *Moore and Keller* [1990, 1991] provide a reasonable fit to the data over the range of rock diameters from 0.2 to 0.4 m, but significantly overestimates the cumulative area covered by rocks smaller than 0.2 m and larger than 0.4 m. Comparison of our lognormal-modeled distributions with the actual data is very satisfying. With correlation coefficients $r \geq 0.98$ for all landing sites, our lognormal least squares fitting procedure appears to be as good as the exponential least squares procedure of *Golombek and Rapp* [1997]. Similarly to exponential-modeled distributions, our lognormal-modeled distributions establish a family of non-crossing curves that flatten out at small rock diameter. However, contrary to exponential-modeled distributions, our lognormal-modeled distributions are able to reproduce correctly both the smallest and the biggest rock size ranges.

5.2. Rock Size-Frequency Distributions for Earth-Analogue Sites

[49] The rock size-frequency distributions found on Mars can be compared with rock size-frequency distributions for a variety of rocky sites found in the McMurdo Dry Valleys, a hyper-arid cold desert that forms the largest ice-free area of the Antarctic continent and is considered a preferential area to understand aeolian processes occurring in many rocky, unvegetated and hyper-arid deserts on Earth, as well as on Mars [*Lancaster*, 2004]. Indeed, strong winds that transport sediments of sand and dust size (1000 μm to 2 μm) are an important feature of this environment and evidence for aeolian processes is therefore widespread throughout the McMurdo Dry Valleys. A total of 17 sites were selected by *Lancaster* [2004] in the McMurdo Dry Valleys for studying wind profile parameters and surface roughness characteristics. These sites were selected to span a range of roughness, from sand sheets to boulder-covered moraines, and so as to be relatively homogenous and have low relief and surface slope. Further information summarizing the characteristics and locations of the sites can be found in the work of *Lancaster* [2004, Table I].

[50] Figure 11 reports the results of our lognormal least squares fitting procedure on the rock distributions, displayed as the number of rocks of each diameter, at different analog sites investigated in the McMurdo Dry Valleys whose rock abundance span the entire range of terrains investigated by *Lancaster* [2004]: Wright Valley 3 (smooth site), Lake Fryxell 3 (moderately rough site) and Lake Hoare (rough site). With correlation coefficients $r \geq 0.95$ for most studied cases, our lognormal least squares fitting procedure appears quite good and provides a satisfying fit for all rock size classes. Figure 12 displays the cumulative fractional area covered by rocks with diameters greater than D versus rock diameter D for the same analog sites investigated in the McMurdo Dry Valleys, along with the different theoretical distributions that have been suggested to describe them. As for the Mars landing sites, comparison of our lognormal-modeled distributions with the actual data is quite satisfying. Again, with correlation coefficients $r \geq 0.97$ for most studied cases, our lognormal least squares fitting procedure appears indeed to be as good as the exponential least squares fitting procedure of *Golombek and Rapp* [1997]. The lack of satisfying solutions for a limited number of sites (Wright Valley 1 and Victoria Valley 2 for which the correlation could not be performed, and Lake Joyce 3 for which $r = 0.78$) demonstrates however that the flexibility of our lognormal-modeled distributions is somewhat limited. It is worth pointing out here that arid and semi-arid terrestrial areas

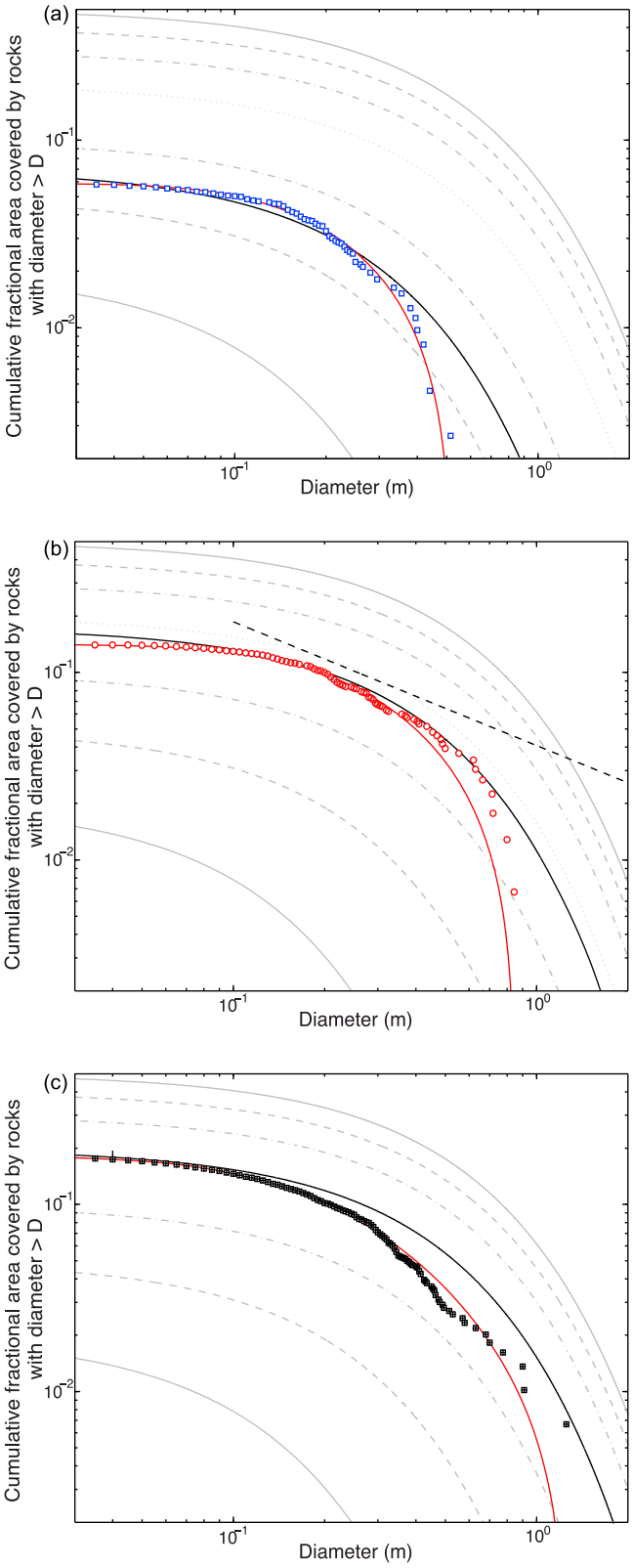

Figure 10. Cumulative fractional area covered by rocks greater than diameter D versus rock diameter D for the near fields of the (a) VL1, (b) VL2, and (c) MPF landing sites. Red lines correspond to the lognormal-modeled distributions for the same sites as derived in section 5.1 of this paper. Straight dashed line corresponds to the power law–modeled distribution for the VL2 landing site suggested by *Moore and Jakosky* [1989] and *Moore and Keller* [1990, 1991] for rocks with diameters $D > 0.1$ m. Black lines correspond to the exponential-modeled distributions for the same sites as derived by *Golombek and Rapp* [1997]. Grey lines correspond to the generalized exponential-modeled distributions for 2.5%, 5%, 10%, 20%, 30%, 40% and 50% rock abundances as derived by *Golombek and Rapp* [1997].

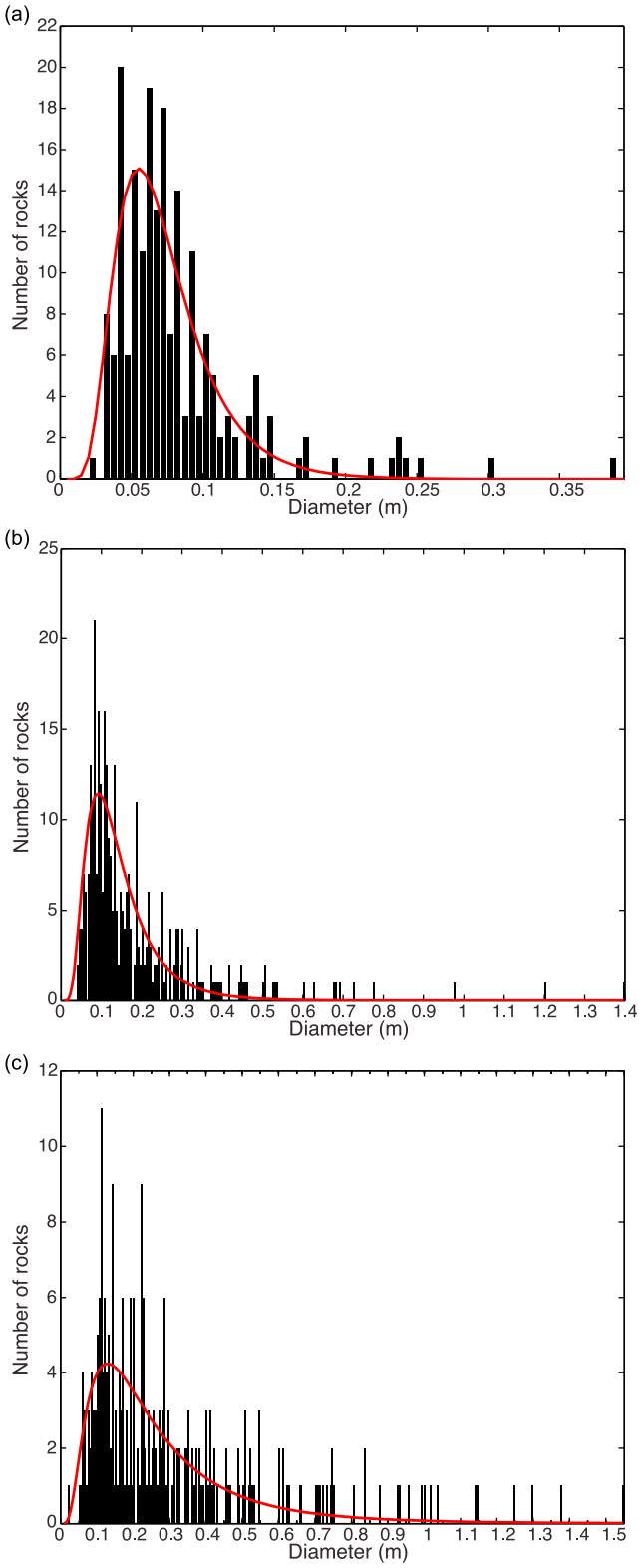

Figure 11. Number distribution of rocks versus diameter at representative analog sites investigated in the (a) McMurdo Dry Valleys, Antarctica: Wright Valley 3 - smooth site, (b) Lake Fryxell 3 - moderately rough site, and (c) Lake Hoare - rough site (binned to a resolution of a half centimeter) along with our lognormal-modeled distributions for the same sites.

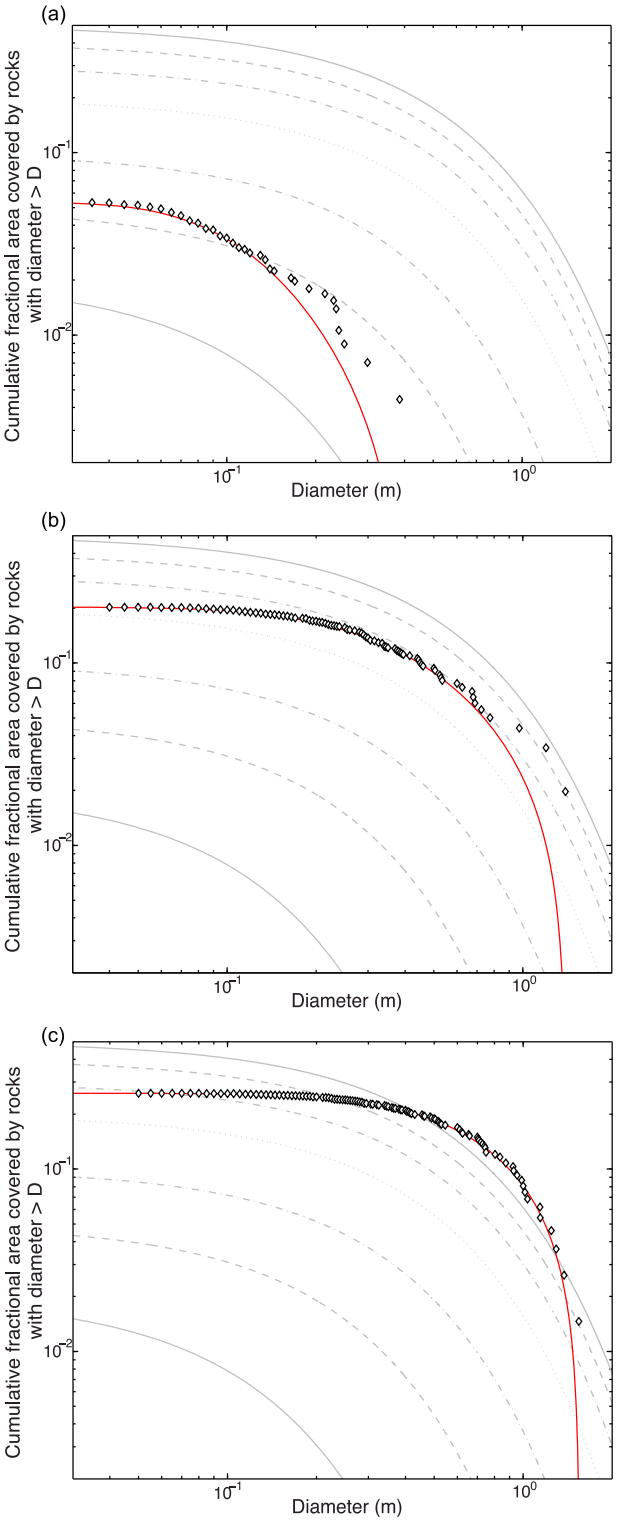

Figure 12. Cumulative fractional area covered by rocks greater than diameter *D* versus rock diameter *D* at (a) Wright Valley 3 - smooth site, (b) Lake Fryxell 3 - moderately rough site, and (c) Lake Hoare - rough site. Red lines correspond to the lognormal-modeled distribution for the same sites as derived in section 5.2 of this paper. Grey lines correspond to the generalized exponential-modeled distributions for 2.5%, 5%, 10%, 20%, 30%, 40% and 50% rock abundances as derived by *Golombek and Rapp* [1997].

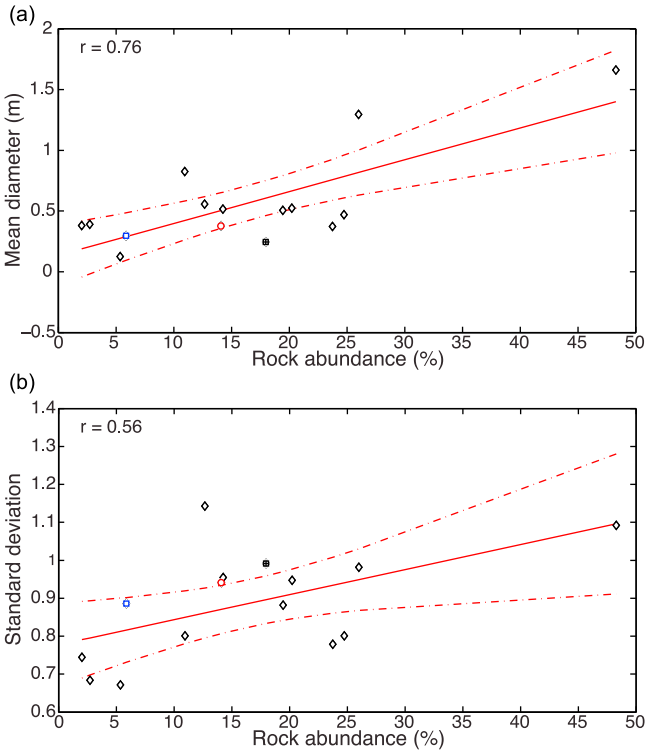

Figure 13. Relation between the (a) mean diameter e^{μ} and (b) standard deviation σ of our fitted lognormal distributions for a rock abundance ζ. Plain red line corresponds to the best linear fit applied to the entire set of rock populations. Dash red lines correspond to the 2-σ uncertainty in our linear regression. Blue, red and black points correspond to the VL1, VL2 and MPF landing sites in situ data sets, respectively.

subjected to dust erosion often exhibit a bimodal size distribution [*Chatenet et al.*, 1996]. It would have been therefore possible to base our procedure on the fitting of two lognormal distributions (each characterized by an amplitude, a median diameter and a standard deviation, i.e. six independent parameters for a two-component distribution) to the observed values by minimizing the difference between the simulated and observed rock populations. But then, it would have been quite hazardous to generalize each of these parameters to the whole Martian surface with the limited amount of available data at our disposal. For this purpose, in the frame of this study, we preferred therefore to stick with our monomodal distribution.

5.3. Generalized Rock Size-Frequency Distributions

[51] The data gathered at some Martian landing sites, as well as the data collected from different Earth-analog sites, suggest that the statistical characteristics (median diameter e^{μ} and standard deviation σ) for any rock population and used in the lognormal fitting expressed by equations (20) and (21) might be roughly related to its total rock abundance ζ. By assuming that there is a smooth variation in both the $f_{\zeta}(D, \mu_N(\zeta), \sigma_N(\zeta))$ and $F_{\zeta}(D, \mu_A(\zeta), \sigma_A(\zeta))$ distributions between different values of ζ, we aimed at extrapolating our previous results to any value of rock abundance ζ. After a simple linear fitting procedure applied to the entire set of rock populations, the results were:

$$e^{\mu_A} = 2.62 \times \zeta + 0.14 \ (\mathrm{r} = 0.76) \tag{22}$$

$$\sigma_A = 0.66 \times \zeta + 0.78 \ (\mathrm{r} = 0.56) \tag{23}$$

[52] Figure 13 displays these parameters derived from the rock-size frequency distributions at every site we considered. It establishes relatively satisfying relationships between both the median diameter e^{μ} and the standard deviation σ of our lognormal-modeled distributions with the total rock abundance ζ, with correlation coefficient r values of 0.76 and 0.56, respectively. We were therefore able to derive the generalized equation

$$F_{\zeta}(D, \mu_A(\zeta), \sigma_A(\zeta)) = \zeta\left(\frac{1}{2} + \mathrm{erf}\left[-\frac{\ln D - \mu_A}{\sigma_A\sqrt{2}}\right]\right),$$

where $F_{\zeta}(D, \mu_A(\zeta), \sigma_A(\zeta))$ is the cumulative fractional area covered by rocks of diameter D or larger, ζ is the total rock abundance, and $\mu_A(\zeta)$ and $\sigma_A(\zeta)$ are, respectively, the median diameter and the standard deviation of our lognormal-modeled rock distribution associated with the total rock abundance ζ. Our generalized lognormal-modeled distributions are noncrossing, i.e. there are unequivocal bijective relationships between $\mu_A(\zeta)$, $\sigma_A(\zeta)$) and ζ. Our generalized lognormal-modeled distributions are also of a globally similar shape to what is observed for the Martian landing sites and different Earth-analog sites as well, i.e. the generalization of several lognormal-modeled distributions remains a lognormal-modeled distribution. It is therefore legitimate to generalize these distributions to the whole surface of Mars. Figure 14 displays the cumulative

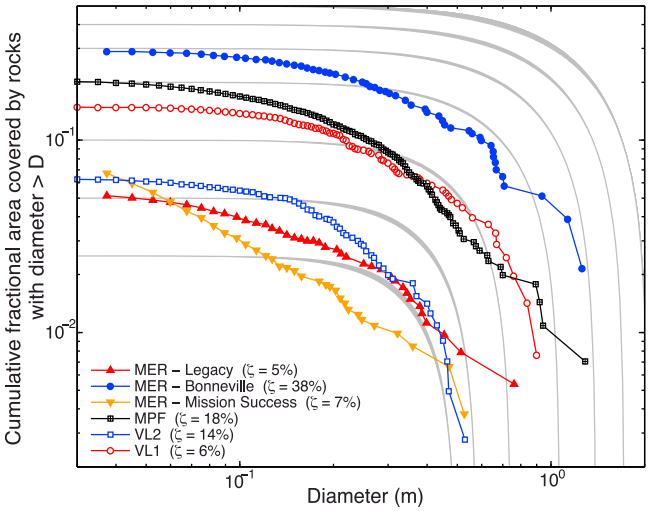

Figure 14. Rock size-frequency distributions at three locations along the Spirit traverse, VL1, VL2 and MPF landing sites. Solid grey lines display our generalized lognormal-modeled distributions for 2.5%, 5%, 10%, 20%, 30%, 40% and 50% rock abundances along with their estimated 2-σ regression uncertainties (adapted from *Golombek et al.* [2005]).

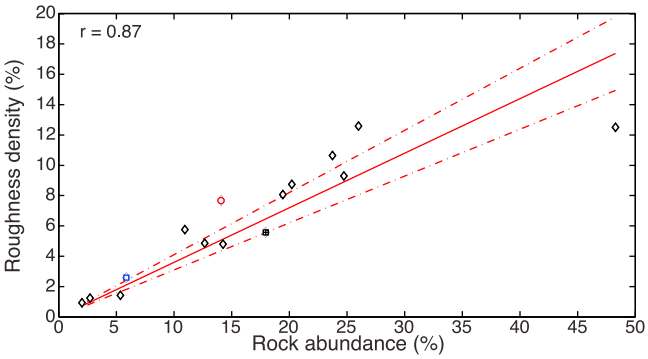

Figure 15. Relation between the roughness density λ and the rock abundance ζ. Plain red line corresponds to the best linear fit applied to the entire set of rock populations. Blue, red and black points correspond to the VL1, VL2 and MPF landing sites in situ data sets, respectively.

fractional area covered by rocks with diameters greater than D versus rock diameter D observed at the different landing sites (adapted from *Golombek et al.* [2005]) along our generalized lognormal-modeled distributions for a large diversity of regularly spaced total rock abundances ζ. The observed rock size-frequency distributions globally follow our lognormal-modeled distributions for the total rock abundances observed at the five respective visited sites on Mars. However, our generalized lognormal-modeled distributions do not compare with the observations as satisfyingly as the corresponding observationally derived lognormal distributions (Figures 10 and 12). This emphasizes the difficulty to rely on increasingly indirect input data to generalize in situ ground-truth results to the whole surface of Mars.

[53] For every site, the total roughness density λ was plotted against the total rock abundance ζ in Figure 15. The best fit was a linear least squares giving:

$$\lambda = 0.3596 \times \zeta \,(\mathrm{r} = 0.87) \tag{24}$$

Equation (24) establishes a generalized relationship that forces the overall shape of the roughness elements to vary proportionally with the total rock abundance ζ with a correlation coefficient r values of 0.87.

[54] Moreover, by assuming a semi-ellipsoidal shape for the roughness elements, equations (12) and (13) give $\lambda = H_m/D_m \times \zeta$. Equation (24) would thus imply that $H_m/D_m = 0.3596$ everywhere, i.e. that rocks tend to be generally roughly as high as they are wide, no matter how rocky the site is. Actual values of H_m/D_m range between 0.26 and 0.54 which is to be compared with a value of 0.5 for hemispherical roughness elements (where $d_i = 2h_i$). For every site, the generalized mean diameter D was plotted against the total rock abundance ζ in Figure 16. The best fit was a linear least squares giving:

$$D_m = 1.369 \times \zeta + 0.158 \;(\mathrm{r} = 0.82) \tag{25}$$

Equation (25) establishes a generalized relationship that forces the generalized mean diameter D of any population of roughness elements to vary proportionally with the total rock abundance ζ with a correlation coefficient r values of 0.82.

[55] Equations (12), (13), (24), and (25) imply finally:

$$H_m = 0.492 \times \zeta + 0.057 \tag{26}$$

By assuming a semi-hemispherical shape for the roughness elements on the surface of Mars, the generally good relations obtained above show clearly that the roughness elements geometry and density are related: the roughness density λ, the generalized mean diameter D_m and the generalized mean height H_m of the roughness elements can all be estimated as a function of the rock abundance ζ. Knowing the rock abundance ζ, it is thus possible to derive these parameters and introduce them into equations (17) and (18) to infer the aerodynamic roughness length associated to the rock populations in question.

$$\text{For } \zeta < 0.1135 \; z_0 = 58.90 \times \zeta^{2.31} + 6.82 \times \zeta^{1.31} \tag{27}$$

$$\text{For } \zeta \geq 0.1135 \; z_0 = 3.40 \times \zeta + 0.39 \tag{28}$$

6. Aerodynamic Roughness Length z_0 on Mars

6.1. A Critical View

[56] Equations (27) and (28) can be applied to any rock abundance data ζ, either measured directly in situ or derived remotely. From the poleward extension of the MGS-TES rock abundance global map, we were able to derive an extended map of the aerodynamic roughness length, at the fullest 1/1° × 1/1°resolution, up to 87° and 87°S latitudes. This extended map of the aerodynamic roughness length is shown in Figure 17. There are different sources of uncertainty that affect this final modeled aerodynamic roughness length values: (1) inaccuracies due to erroneous assumptions in the semi-empirical physical model, (2) imprecisions due to the need to generalize localized in situ observations to the whole surface of Mars, (3) imprecisions due to undetected inter-annual or seasonal changes in the input rock abundance data [*Nowicki and Christensen*, 2007], (4) imprecisions due to the need to extrapolate where the input rock abundance data are absent. The first two sources are discrepancies that could exist between the modeled

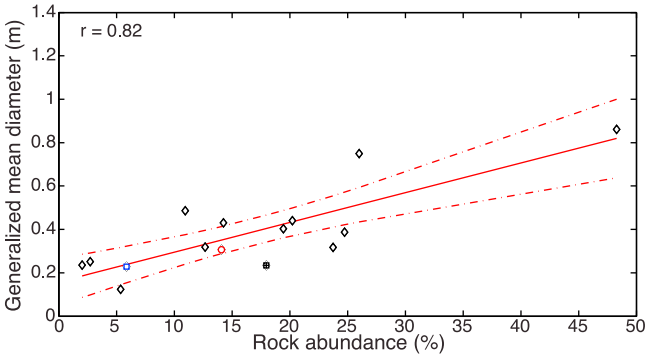

Figure 16. Relation between the generalized mean diameter D and the rock abundance ζ. Plain red line corresponds to the best linear fit applied to the entire set of rock populations. Blue, red and black points correspond to the VL1, VL2and MPF landing sites in situ data sets, respectively.

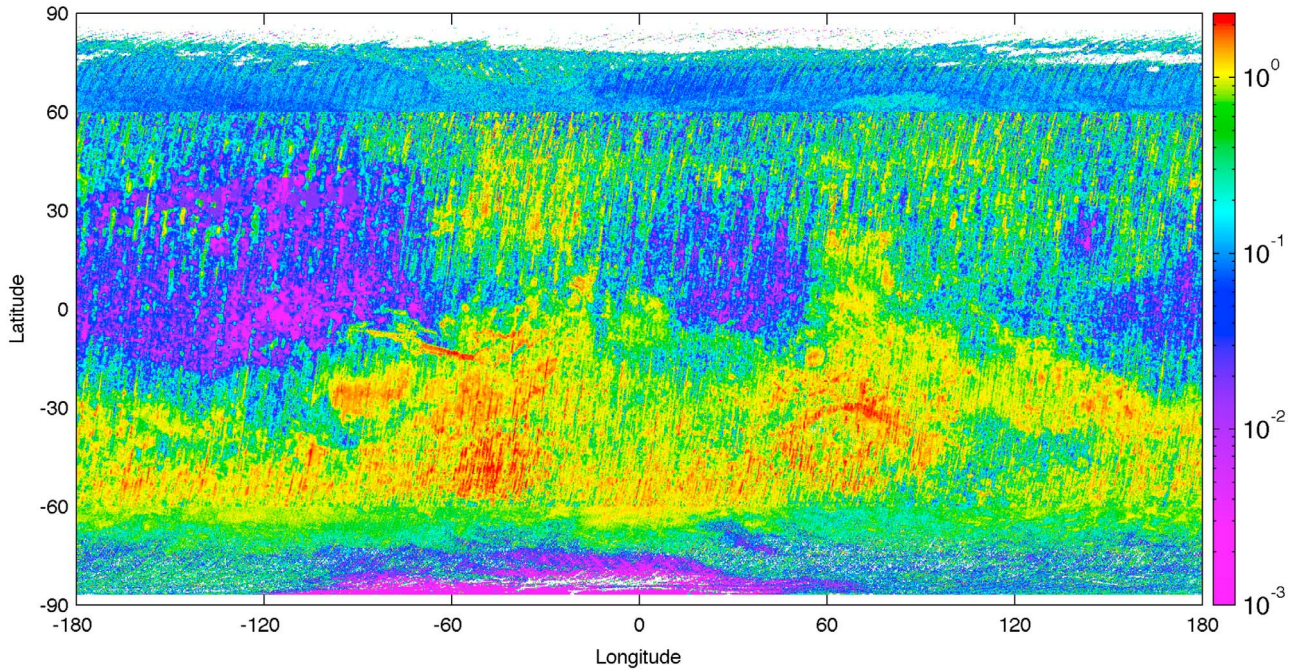

Figure 17. Extended aerodynamic roughness length z_0 (in cm) inferred from MGS-TES rock abundance data with a 1/8° × 1/8° spatial resolution. For the white pixels no values could be derived with our method because of missing inertia and albedo data (poleward of 87°) or because of missing information for [I_k, α_l] bins that are present in the polar regions ([60°N:90°N] and [90°S:60°S]) but missing from the [60°S:60°N] reference region. These pixels mainly correspond to areas of exposed ice sheets.

values and the actual conditions of the considered surface of Mars. It is difficult to estimate their extent without a validation based on ground-truth data. The latter sources of uncertainty are directly related to the uncertainties $\Delta\zeta$ attached to the original rock abundance data and to their extrapolated values at high latitudes. They both have been previously outlined and estimated in detail, either in *Nowicki and Christensen*'s [2007] article or in section 4.5 of this

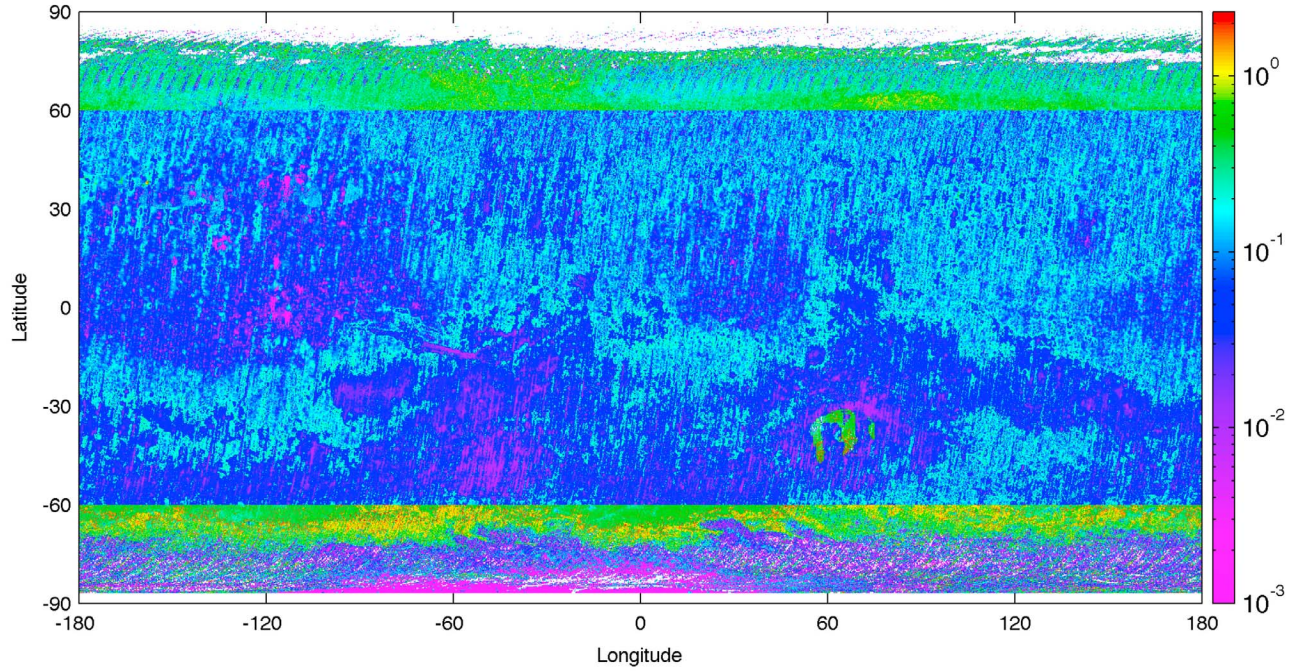

Figure 18. Uncertainty Δz_0 attached to the aerodynamic roughness length z_0 (in cm) inferred from the extended MGS-TES rock abundance data with a 1/8° × 1/8° spatial resolution.

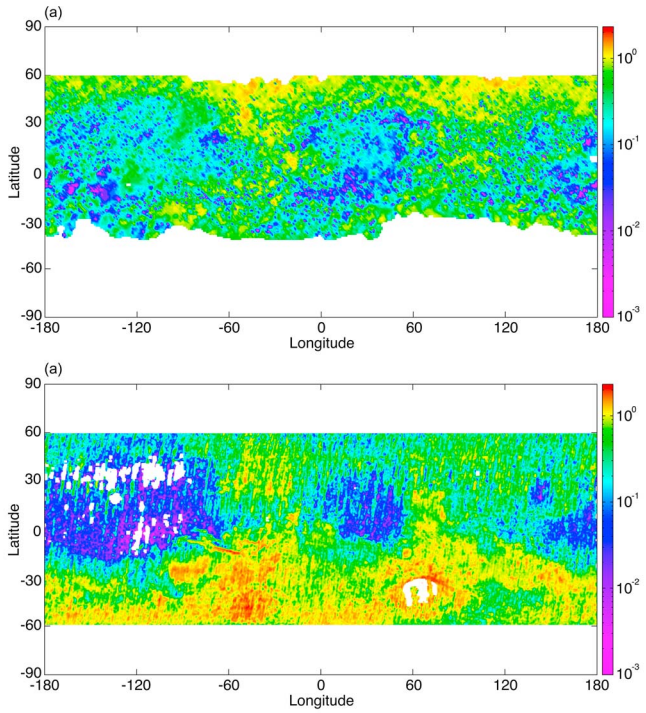

Figure 19. Comparison of aerodynamic roughness length z_0 (in cm) inferred from (a) Viking-IRTM rock abundance data and (b) MGS-TES rock abundance data convolved to ($1/1° \times 1/1°$ spatial resolution).

paper. These are significantly large errors. We illustrate in Figure 18 a critical regard of their effect on the final calculated aerodynamic roughness length. We derived an overall uncertainties Δz_0 from a propagation of the rock abundance uncertainties $\Delta\zeta$ in equations (27) and (28).

6.2. Intercomparison of Aerodynamic Roughness Length z_0 Data Sets

[57] Equations (27) and (28) can be applied both to the Viking-IRTM and MGS-TES rock abundance data ζ. A direct comparison between the aerodynamic roughness lengths derived from these two data sets is difficult considering the differences in spatial resolution and sampling of observations [*Christensen*, 1986; *Nowicki and Christensen*, 2007]. MGS-TES rock abundance data are averaged to $1/1° \times 1/1°$ spatial resolution and a significant fraction of the area included in the bin is not observed (Figure 19). Despite the differences in spatial resolution and sampling of observations, the agreement between the aerodynamic roughness lengths derived from the Viking-IRTM and MGS-TES data sets is good. Such agreement was expected since it was already fulfilled when comparing the original Viking-IRTM and MGS-TES rock abundance data sets (see *Nowicki and Christensen* [2007] for a detailed discussion). The smoother and rougher regions match in both maps and, generally, the large-scale patterns exhibited by the aerodynamic roughness length agree on the global scale. The higher occurrences of both rougher ($z_0 > 1$ cm) and smoother surfaces ($z_0 < 0.01$ cm) in MGS-TES data was expected, considering the higher resolution of the MGS-TES rock abundance data.

[58] A few recent in situ data sets have become sufficient these past years to motivate the use of empirical relationships between the aerodynamic and geometric roughnesses on Mars. The six Mars landing sites (Viking landers 1 and 2, Mars PathFinder, MER-A Spirit, MER-B Opportunity and Phoenix Mars Lander) are the only points of reference for directly relating remotely observed aerodynamic roughness length to any in situ information about the geometric roughness. In these specific locations of the Martian surface, some indirect estimations and/or direct measurements of the aerodynamic roughness length have been performed along with its corresponding local geometrical characteristics. For

Table 1. Aerodynamic Roughness Length Values (in cm) Inferred From Our Processing of Viking-IRTM, MGS-TES and In Situ Estimations of Rock Abundance Data Compared to Direct Measurements and/or Other Estimations

Landing Site	Viking-IRTM[a]	MGS-TES[b]	In Situ Estimations	Direct Measurements or (Other Estimations)
Viking 1	0.94	0.42 ± 0.19	0.25[c]	(0.1–1.0)[d]
Viking 2	0.97	0.84 ± 0.14	0.87[c]	(0.1–1.0)[d]
Mars PathFinder	1.04	0.80 ± 0.14	1.01[e]	3.00[f]
MER-A Spirit	0.42	0.74 ± 0.14	0.34[g]	(0.14)[h]
MER-B Opportunity	0.19	0.52 ± 0.26	≤0.19[g]	NA
Phoenix Mars Lander	NA	0.03 ± 0.17	≤0.19[i]	0.6 ± 0.3 / 0.5 ± 0.3[j]

[a]Viking-IRTM rock abundances were calculated by *Christensen* [1986] and were selected for landing site hazard assessment and selection studies by *Golombek and Rapp* [1997] and *Golombek et al.* [1999, 2003, 2005]. Viking-IRTM observations were restricted between latitudes 60°S and 60°N due to seasonal frost and atmospheric conditions, and are therefore not available for Phoenix landing site.

[b]MGS-TES rock abundances (and their associated uncertainties) were calculated by *Nowicki and Christensen* [2007] and were selected for landing site hazard assessment and selection studies by *Golombek et al.* [2008]. MGS-TES observations were restricted between latitudes 60°S and 60°N due to seasonal frost and atmospheric conditions, and we relied upon our rock abundance extrapolation methodology to derive the aerodynamic roughness length z_0 for Phoenix landing site.

[c]At Viking 1 and 2 landing sites, rock abundances were estimated by *Moore and Jakosky* [1989] and *Moore and Keller* [1990, 1991].

[d]As estimated by *Sutton et al.* [1978].

[e]At Mars PathFinder landing site, rock abundances were estimated by *Yingst et al.* [2007].

[f]As measured by *Sullivan et al.* [2000].

[g]At the MER-A Spirit and MER-B Opportunity landing sites, rock abundances were estimated by *Grant et al.* [2006].

[h]As estimated by *Greeley et al.* [2008].

[i]At Phoenix landing site, rock abundances were estimated by *Heet et al.* [2009].

[j]As measured by *Holstein-Rathlou et al.* [2010].

each site, all available rock abundance data were compiled and used for estimating the aerodynamic roughness length according to the methodology described above. Results are displayed in Table 1.

[59] First, comparisons are made between the aerodynamic roughness length we derived at these sites from binned 1 pixel/degree Viking-IRTM and 8 pixels/degree MGS-TES rock abundance data sets. Viking-IRTM rock abundance values were presented by *Christensen* [1986] and were selected for further landing site hazard assessment and selection studies by *Golombek and Rapp* [1997] and *Golombek et al.* [1999, 2003, 2005]. While three of the six sites were observed directly with MGS-TES, those for Viking Lander 1, MER-B Opportunity and Phoenix Mars Lander were not. Rock abundance values for both VL1 and MER-B were interpolated by *Nowicki and Christensen* [2007] from surrounding pixels to provide a rough estimate of the local surface rock abundance, although the actual site had not been observed. The rock abundance value at Phoenix landing site was derived using our own extrapolation technique (see section 4). One should keep in mind that the spatial scale of the orbiter observations is ∼60 km for Viking-IRTM and ∼7.5 km for MGS-TES, whereas the landers are only on the order of 10 m [*Moore and Keller*, 1990, 1991; *Golombek et al.*, 2003, 2005]. Then, we derived the aerodynamic roughness length from the best estimate rock counts performed on visible images [*Moore and Jakosky*, 1989; *Moore and Keller*, 1990, 1991; *Grant et al.*, 2006; *Yingst et al.*, 2007; *Heet et al.*, 2009]in these locations. Finally, the last column of Table 1 displays the aerodynamic roughness length values that have been either estimated from the Viking landers and MER-A Spirit images [*Sutton et al.*, 1978; *Greeley et al.*, 2008]through the relation previously suggested by *Lettau* [1969] ($z_0 = \lambda/2$) or have been measured directly through exhaustive wind profiles analysis during Mars PathFinder and Phoenix Mars Lander operations [*Sullivan et al.*, 2000; *Holstein-Rathlou et al.*, 2010]. The field measurements performed during these last two missions consisted of the only direct measurements of near-surface wind profiles, including the determination of the wind friction speeds and the aerodynamic roughness length, ever made on Mars. This was accomplished by the Imager for Mars PathFinder (IMP) windsock experiment and by the Telltale wind indicator through the measurement of wind speeds at different heights above the Martian surface during Mars PathFinder and Phoenix Mars Lander operations, respectively. The IMP windsock experiment aboard Mars PathFinder measured wind speeds at three heights within 1.2 m of the Martian surface. These wind data allowed *Sullivan et al.* [2000] to measure directly the near-surface wind profiles on Mars for the first time and therefore to characterize the local aeolian properties. Winds were light during periods of windsock imaging, but data from the strongest breezes indicated an aerodynamic roughness length $z_0 \sim 3$ cm at the landing site, and wind friction velocities u^t reaching 1 m.s^{-1}. Results reported by Mars PathFinder were therefore slightly above the previous assumptions regarding an overall aerodynamic roughness length on Mars which typically ranged from 0.1 cm to 1 cm [*Sutton et al.*, 1978]. Nevertheless, they still seemed reasonably consistent because the PathFinder landing site was believed to be significantly rockier and rougher than most typical plains units elsewhere on Mars. Using the Telltale wind indicator, *Holstein-Rathlou et al.* [2010] were able to derive two different aerodynamic roughness lengths z_0 at Phoenix landing site, situated in the northern polar region (68.22°N, −125.75°W), by measuring the strength of the 3 Hz turbulence through the blurring of the instrument and by studying the wind stability at nighttime. Both methods gave roughly the same estimates, 6 ± 3 mm and 5 ± 3 mm, respectively, which were lower than previous estimates for Mars PathFinder and Viking landing sites. Such a result was expected as the Phoenix landing site seems, on the contrary, depleted in rocks of all sizes relative to these previous landing sites [*Heet et al.*, 2009].

[60] The match between the aerodynamic roughness length values inferred from (i) MGS-TES remote sensing and (ii) in situ derived rock abundances is quite good considering the difference in spatial scales. Even if we cannot perfectly explain quantitatively all the values suggested by these different techniques, our results agree qualitatively in terms of orders of magnitude and relative differences (from ∼4% to ∼74% for Viking Lander 2 and MER-A Spirit landing sites, respectively). More precisely, the in situ estimations from most of the landers lie within the range defined by our treatment of MGS-TES observations and their associated uncertainties, except for MER-A Spirit. We emphasize once again that local meter-length scale phenomena could not have been resolved by the MGS-TES resolution anyway, or by Viking-IRTM. At the Viking and MER-A Spirit landing sites, our derived values are quite comparable to the estimations previously made [*Sutton et al.*, 1978; *Greeley et al.*, 2008]. We were however unable to reproduce exactly the aerodynamic roughness length values measured by Mars PathFinder and Phoenix. The matching of our derived aerodynamic roughness length values to the range of local values recently measured at the Phoenix landing site by *Holstein-Rathlou et al.* [2010], each within their respective range of uncertainties (above 50%), lends some limited confidence not only in our model of rock size-frequency distributions but in our extrapolation technique as well. Wind conditions during Mars PathFinder lander operations were light, resulting in most data being unsuitable for a rigorous analysis of the wind profile [*Sullivan et al.*, 2000]. Short periods of stronger breezes, however, deflected the windsocks sufficiently to report an aerodynamic roughness length $z_0 = 3$ cm at the landing site. Considering the wind conditions during Mars PathFinder landing operations and the extent of the uncertainties reported by *Holstein-Rathlou et al.* [2010] for Phoenix (above 50%), we can reasonably expect this value to be associated with large relative uncertainties as well. Moreover, such an observed value is considered to be unusually high for plains [*Sullivan et al.*, 2000] and we derived for this landing site different values of z_0 ranging from 0.66 to 1.04 cm, much closer to what could be expected from the rockiest sites available in our database.

[61] These results indicate that Mars is actually more spatially heterogenous than has been assumed before, at least from an aerodynamic roughness standpoint. The Martian aerodynamic roughness length we derived from MGS-TES observations varies from 10^{-3}cm to 2.334 cm. It stretches over a broader range of values than what has been recently

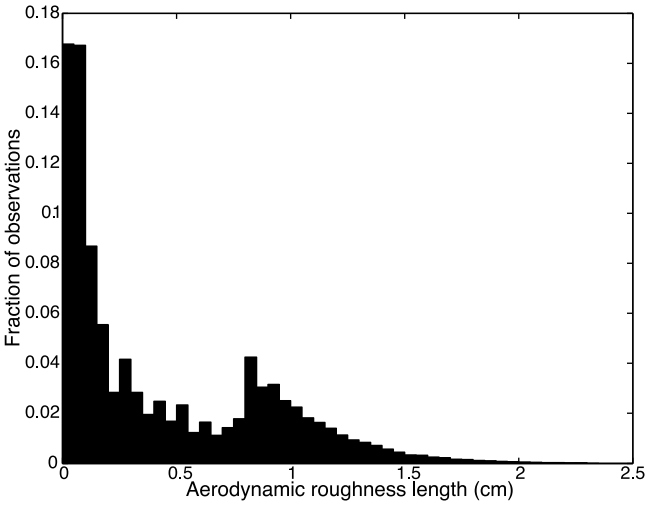

Figure 20. Histogram of the aerodynamic roughness length z_0 values inferred from MGS-TES rock abundance data with a 1/8° × 1/8° spatial resolution (binned to a resolution of a half millimeter).

reported by *Heavens et al.* [2008]. By using high-resolution laser altimetry from MGS-MOLA, they succeeded in deriving two different spatially variable aerodynamic roughness length maps ranging from 2×10^{-2} cm to 16.62 cm and from 1 cm to 10 cm, respectively. The histogram of the resulting 8 pixel/degree aerodynamic roughness length data set exhibits a bimodal distribution with maxima at $5 \times 10^{-3} - 10^{-2}$ cm and 0.80–0.85 cm, with an average of 0.44 cm globally (Figure 20). At this fullest resolution and 0.5 mm bin size, about 84% of the Martian surface is characterized by an aerodynamic roughness length value lower than the spatially uniform value $z_0 = 1$ cm that many MGCM simulations have often assumed so far [*Newman et al.*, 2002a, 2002b, 2005; *Kahre et al.*, 2005, 2006, 2008; *Spiga and Lewis*, 2010]. About 11% of the Martian surface is characterized by an aerodynamic roughness length value higher than $z_0 = 1$ cm. About 5% of the Martian surface is indeed characterized by a value z_0 comprised in the 0.95–1.05 cm range. These results indicate that the methodology developed and applied in this research project to estimate the aerodynamic roughness length provides a reasonable picture of its nature on Mars and suggests that the map we have derived at the fullest resolution available will be crucial to characterize local aeolian features. Whatever the approach, ours or any other described briefly in this paper, the estimation of the aerodynamic roughness length relies on some empirical relationships between a few limited sets of ground-truth field measurements and some geometrical roughness characteristics of the surface, determined either in situ or remotely. Their practical application on a global scale remains therefore quite questionable [*King et al.*, 2005].

6.3. Aerodynamic Roughness Length z_0 for the Exposed Ice Sheets

[62] In the new mapping of the aerodynamic roughness length we have derived up to high latitudes, there still remain missing values. First, values could not be derived above 87°N and 87°S due to a lack of thermal inertia and albedo data at these high latitudes. Secondly, below these latitudes and above 80°N and 80°S high thermal inertia values prevented us from extrapolating any value of rock abundance from the [60°N, 60°S] reference region. These high thermal inertia values correspond to the exposed ice sheets on the North polar cap and, to a lesser extent, on the South polar cap. As observed by the Mars Orbiter Camera (MOC) onboard Mars Global Surveyor (MGS) (see, e.g., *Malin and Edgett* [2001, Figure 76] for the North Polar cap and *Malin and Edgett* [2001, Figure 100] for a global overview of exposed ice sheets at the Martian surface), the thin layers of missing values observed in the northern polar region map exactly the exposed ice sheets whereas these local icy regions cover only the [−150°E:15°E] region below 84°S latitude in the southern polar region. Since our intent was to provide a full map as an input for MGCMs, it was mandatory to fill in the gaps by taking into account the local icy surface morphologies in these peculiar regions.

[63] To do so, we first reviewed the observations of the surfaces features available for both northern and southern polar regions; the northern residual cap is characterized by a rough surface made up of pits, knobs, and linear depressions on scales of tens of meters [*Milkovich et al.*, 2010] whereas the southern cap exhibits greater structures, with sizes ranging from about ten meters to a few hundreds of meters [*Malin and Edgett*, 2001]. Indeed, MGS-MOC provided images showing differences in surface textures of both polar caps [see *Malin and Edgett*, 2001, Figure 62] which suggest wider depressions in the South polar cap than in the North polar cap. However, the aerodynamic roughness length describes micro-scale roughness features much smaller than the meso-scale morphological features that such imaging of the polar caps can resolve. For that reason it is not relevant to suggest a different value of z_0 relying on these observed meso-scale differences and we chose to keep instead a similar value for both poles. As a matter of fact, the values we successfully derived for the aerodynamic roughness length at the North and South polar caps (as close as possible to the 87°N and 87°S latitudes) are globally quite similar. Investigations of the turbulent transfer in terrestrial polar regions and mountain glaciers indicated that $z_0 = 0.01$ to 1 cm over snow and ice [*Calanca*, 2001, and references therein]. Values outside this range seem to be observed either over very smooth ice surfaces or in the presence of snow drifts. Thus, the moderately rough texture observed in these Martian polar terrains allowed us to apply $z_0 = 0.1$ cm wherever ice was present. In the southern hemisphere, some areas which remained unfilled could not be reasonably connected to ice sheets. These areas can be related to areas where seasonal deposition may occur but whose corresponding MGS-TES observations have been averaged over different seasons with different amounts of ice deposition. To determine which pixels corresponded to ice and which did not in these regions, we roughly estimated the main region of the permanent south polar ice cap as being located between −150°E and 30°E in longitude and 87°S and 90°S in latitude, with a smaller extension added up to latitude 84°S, between −115°E and 15°E which covers an area where seasonal deposition occurs.

[64] Regions at latitudes poleward of 87°S but outside the longitude range of the southern cap were given a default value corresponding to the mean rock abundance value found at the 87°S border. The few remaining pixels identified as

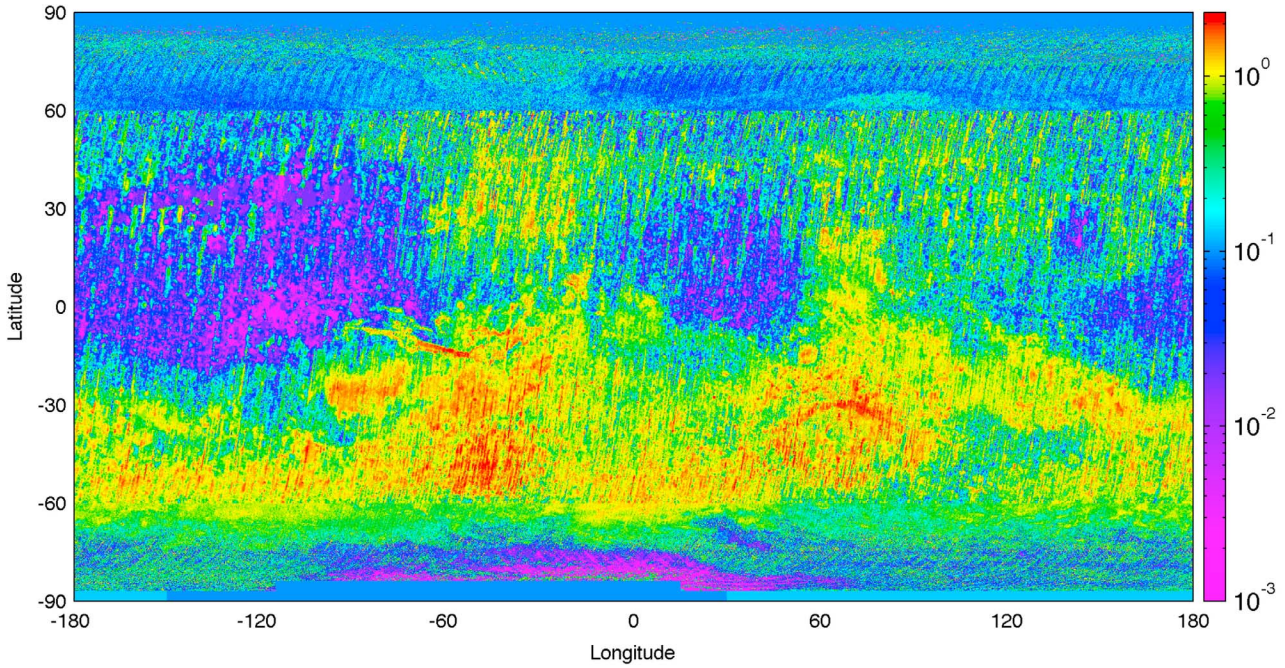

Figure 21. Completed aerodynamic roughness length z_0 (in cm) inferred from MGS-TES rock abundance data with a 1/8° × 1/8° spatial resolution. A default aerodynamic roughness length value of z_0 = 0.1 cm (sky blue) was given to areas identified as ice sheets. Pixels below 87°S latitude and not related to the south polar ice cap were filled were filled by convoluting the previously extrapolated rock abundance map with an inverse distance-weighted mean over a centered (3 × 3 pixels)-sized kernel. Pixels poleward of 87°S but outside the longitude range of the south polar ice cap were given a default value corresponding to the mean rock abundance found at the 87° border.

not being related to ice with latitudes below 87°S were filled by convoluting the previously extrapolated rock abundance map with an inverse distance-weighted mean over a centered (3 × 3 pixels)-sized kernel. By working with this smallest possible kernel, we could still account as much as possible for the local geomorphologies. The complete map we finally obtained is shown in Figure 21.

7. Conclusion

[65] We have established a map of the aerodynamic roughness length z_0 over the entire Martian surface. We have chosen to use rock abundance data sets to develop a high-resolution mapping of this parameter, rather than extrapolating the limited amount of ground-truth data to infer an "idealized" coverage of this parameter. Our methodology was calibrated on the basis of rock-size frequency distributions inferred from different Martian landing sites and Earth analog sites. It was then generalized using extrapolated rock abundance data derived from measurements of the Thermal Emission Spectrometer (TES) aboard Mars Global Surveyor (MGS). We have established that a lognormal distribution allows us to reproduce very well the smallest rocks population which is of great importance in estimating the aerodynamic roughness length. We have validated the hypothesis that the rock abundance of a given area could be estimated at a first order from its thermophysical properties, namely its thermal inertia I and its albedo α. The extrapolation of the rock abundance values is better when considering the thermal inertia and albedo of the closest regions as a reference, because of the higher similarities of geological terrains. Finally, by comparing with previous measurements and/or estimations made at different landing sites, we have shown that our map gives a realistic overview of the aerodynamic roughness length on Mars. It is the very first attempt at deriving an aerodynamic roughness length map at such a high resolution. One of the major results of this research project is that we were able to map aerodynamic roughness length values that are significantly higher and lower than the one that has been previously used in many MGCM simulations [*Newman et al.*, 2002a, 2002b, 2005; *Kahre et al.*, 2005, 2006, 2008; *Spiga and Lewis*, 2010]. The higher occurrences of both rougher ($z_0 > 1$ cm) and smoother ($z_0 < 1$ cm) surfaces in our map is a direct consequence of the high spatial resolution of the MGS-TES observations used throughout this study, which have proven to be useful to distinguish specific surfaces that may exhibit similar microscale processes. Because of the limited amount of calibration data and some methodological uncertainties we do not claim to give an accurate representation of this parameter on Mars, but only one that spans a plausible range of values to be used in MGCMs, along with the parameterizations needed for using it to estimate the wind erosion threshold velocity.

Notation

z_0 aerodynamic roughness length (m).
z_{0s} aerodynamic roughness length on a smooth surface (m).
α albedo.

ρ atmosphere density (g.cm^{-3}).
$F(D, \mu_A, \sigma_A)$ cumulative fractional area covered by rocks with diameter greater than any diameter D associated with a rock population characterized in fractional area by a median diameter μ_A and a standard deviation σ_A (m^2).
$f(D, \mu_N, \sigma_N)$ number of rocks of any diameter D. associated with a rock population characterized in number by a median diameter μ_N and a standard deviation σ_N.
ρ_d dust particle density (g.cm^{-3}).
f_{eff} effective friction velocity ratio.
f arithmetic mean frontal surface area (m^2).
f_i individual frontal surface area for the individual roughness elements (m^2).
D_m generalized mean diameter (m).
H_m generalized mean height (m).
ν kinematic viscosity (m.s^{-1}).
D_p particle diameter (m).
R_e Reynolds number.
ζ rock abundance (%).
λ roughness density (%).
s_i surface area for the individual roughness elements (m^2).
S total surface area (m^2).
I thermal inertia (J.m^{-2}.K^{-1}.s$^{-1/2}$)
u^t_{drag} threshold wind friction velocity (m.s^{-1}).
u^{ts}_{drag} threshold wind friction velocity on a smooth surface (m.s^{-1}).
u_{drag} wind friction velocity (m.s^{-1}).
τ wind shear stress (Pa).
τ_s wind shear stress on a smooth surface (Pa).
τ^t wind shear stress threshold (Pa).

[66] **Acknowledgments.** We thank Nicholas Lancaster for providing us with the rock data in the McMurdo Dry Valleys. We are grateful to our reviewers, Claire Newman and Robin Fergason, for providing us with particularly detailed and helpful comments during the reviewing process. This work was supported by the Centre National d'Études Spatiales (CNES) and the Institut Pierre-Simon Laplace (IPSL) through postdoctoral position for E.H.

References

Alfaro, S., and L. Gomes (1995), Improving the large-scale modeling of the saltation flux of soil particles in presence of nonerodible elements, *J. Geophys. Res.*, *100*(D8), 16,357–16,366.

Alfaro, S., A. Gaudichet, L. Gomes, and M. Maillé (1997), Modeling the size distribution of a soil aerosol produced by sandblasting, *J. Geophys. Res.*, *102*(D10), 11,239–11,249.

Arya, S. (1975), A drag partition theory for determining the large-scale roughness parameter and wind stress on the arctic pack ice, *J. Geophys. Res.*, *80*(C24), 3447–3454.

Bagnold, R. A. (1941), *The Physics of Blown Sand and Desert Dunes*, 265 pp., Methuen, London.

Bagnold, R. A. (1954), Experiments on a gravity-free dispersion of large solid spheres in a Newtonian fluid under shear, *Proc. R. Soc. London, Ser. A*, *225*(1160), 49–63.

Basu, S., and M. I. Richardson (2004), Simulation of the Martian dust cycle with the GFDL Mars GCME, *J. Geophys. Res.*, *109*, E11006, doi:10.1029/2004JE002243.

Basu, S., J. Wilson, M. Richardson, and A. Ingersoll (2006), Simulation of spontaneous and variable global dust storms with the GFDL Mars GCM, *J. Geophys. Res.*, *111*, E09004, doi:10.1029/2005JE002660.

Cakmur, R. V., R. L. Miller, J. Perlwitz, I. V. Geogdzhayev, P. Ginoux, D. Koch, K. E. Kohfeld, I. Tegen, and C. S. Zender (2006), Constraining the magnitude of the global dust cycle by minimizing the difference between a model and observations, *J. Geophys. Res.*, *111*, D06207, doi:10.1029/2005JD005791.

Calanca, P. (2001), A note on the roughness length for temperature over melting snow and ice, *Q. J. R. Meteorol. Soc.*, *127*, 255–260.

Callot, Y., B. Marticorena, and G. Bergametti (2000), Geomorphologic approach for modelling the surface features of arid environments in a model of dust emissions: application to the Sahara Desert, *Geodin. Acta*, *13*(5),245–270.

Cantor, B. A. (2007), MOC observations of the 2001 Mars planet-encircling dust storm, *Icarus*, *186*(1), 60–96.

Cantor, B. A., P. B. James, M. Caplinger, and M. J. Wolff (2001), Martian dust storms: 1999 Mars Orbiter Camera observations, *J. Geophys. Res.*, *106*(E10), 23,653–23,687.

Cantor, B. A., K. M. Kanak, and K. S. Edgett (2006), Mars Orbiter Camera observations of Martian dust devils and their tracks (September 1997 to January 2006) and evaluation of theoretical vortex models, *J. Geophys. Res.*, *111*, E12002, doi:10.1029/2006JE002700.

Chatenet, B., B. Marticorena, L. Gomes, and G. Bergametti (1996), Assessing the microped size distributions of desert soils erodible by wind, *Sedimentology*, *43*(5), 901–911.

Chepil, W. S. (1945), Dynamics of the wind erosion. I. Nature of movement of soil by wind, *Soil Sci.*, *60*, 305–320.

Christensen, P. R. (1982), Martian dust mantling and surface composition: Interpretation of thermophysical properties, *J. Geophys. Res.*, *87*(B12), 9985–9998.

Christensen, P. R. (1986), The spatial-distribution of rocks on Mars, *Icarus*, *68*(2), 217–238.

Christensen, P. R., et al. (2001), Mars Global Surveyor Thermal Emission Spectrometer experiment: Investigation description and surface science results, *J. Geophys. Res.*, *106*(E10), 23,823–23,871.

De Vries, A. C., W. P. Kustas, J. C. Ritchie, W. Klaassen, M. Menenti, A. Rango, and J. H. Prueger (2003), Effective aerodynamic roughness estimated from airborne laser altimeter measurements of surface features, *Int. J. Remote Sens.*, *24*(7), 1545–1558.

Fergason, R. L., P. R. Christensen, and H. H. Kieffer (2006), High-resolution thermal inertia derived from the Thermal Emission Imaging System (THEMIS): Thermal model and applications, *J. Geophys. Res.*, *111*, E12004, doi:10.1029/2006JE002735.

Garratt, J. R. (1977), Aerodynamic roughness and mean monthly surface stress over Australia, *Tech. Rep. 29*, Commonw. Sci. and Ind. Res. Org., Canberra.

Gillette, D. A., J. Adams, D. Muhs, and R. Kihl (1982), Threshold friction velocities and rupture moduli for crusted desert soils for the input of soil particles into the air, *J. Geophys. Res.*, *87*(C11), 9003–9015.

Gillette, D. A., B. Marticorena, and G. Bergametti (1998), Change in the aerodynamic roughness height by saltating grains: Experimental assessment, test of theory, and operational parameterization, *J. Geophys. Res.*, *103*(D6), 6203–6209.

Gillies, J. A., W. G. Nickling, and J. King (2007), Shear stress partitioning in large patches of roughness in the atmospheric inertial sublayer, *Boundary Layer Meteorol.*, *122*(2), 367–396, doi:10.1007/s10546-006-9101-5.

Gillies, J. A., W. G. Nickling, J. King, and N. Lancaster (2010), Modeling aeolian sediment transport thresholds on physically rough Martian surface: A shear stress partitioning approach, *Geomorphology*, *121*(1–2), 15–21.

Golombek, M., and D. Rapp (1997), Size-frequency distributions of rocks on Mars and Earth analog sites: Implications for future landed missions, *J. Geophys. Res.*, *102*(E2), 4117–4129.

Golombek, M. P., H. J. Moore, A. F. C. Haldemann, T. J. Parker, and J. T. Schofield (1999), Assessment of Mars Pathfinder landing site predictions, *J. Geophys. Res.*, *104*(E4), 8585–8594.

Golombek, M. P., A. F. C. Haldemann, N. K. Forsberg-Taylor, E. N. DiMaggio, R. D. Schroeder, B. M. Jakosky, M. T. Mellon, and J. R. Matijevic (2003), Rock size-frequency distributions on Mars and implications for Mars Exploration Rover landing safety and operations, *J. Geophys. Res.*, *108*(E12), 8086, doi:10.1029/2002JE002035.

Golombek, M. P., et al. (2005), Assessment of Mars Exploration Rover landing site predictions, *Nature*, *436*(7047), 44–48.

Golombek, M. P., et al. (2008), Size-frequency distributions of rocks on the northern plains of Mars with special reference to Phoenix landing surfaces, *J. Geophys. Res.*, *113*, E00A09, doi:10.1029/2007JE003065.

Gomes, L., G. Bergametti, F. Dulac, and U. Ezat (1990), Assessing the actual size distribution of atmospheric aerosols collected with a cascade impactor, *J. Aerosol Sci.*, *21*(1), 47–59.

Grant, J. A., S. A. Wilson, S. W. Ruff, M. P. Golombek, and D. L. Koestler (2006), Distribution of rocks on the Gusev Plains and on Husband Hill, Mars, *Geophys. Res. Lett.*, *33*, L16202, doi:10.1029/2006GL026964.

Greeley, R., and J. D. Iversen (1985), *Wind as a Geological Process on Earth, Mars, Venus and Titan*, Cambridge Univ. Press, New York.

Greeley, R., et al. (1991), Assessment of aerodynamic roughness via airborne radar observations, *Acta Mech.*, *2*, 77–88.
Greeley, R., D. G. Blumberg, J. F. McHone, A. Dobrovolskis, J. D. Iversen, N. Lancaster, K. R. Rasmussen, S. D. Wall, and B. R. White (1997), Applications of spaceborne radar laboratory data to the study of aeolian processes, *J. Geophys. Res.*, *102*(E5), 10,971–10,983.
Greeley, R., G. Wilson, R. Coquilla, B. White, and H. R. (2000), Wind-blown dust on Mars: laboratory simulations of flux as a function of surface roughness, *Planet. Space Sci.*, *48*(12), 1349–1355.
Greeley, R., et al. (2008), Columbia Hills, Mars: Aeolian features seen from the ground and orbit, *J. Geophys. Res.*, *113*, E06S06, doi:10.1029/2007JE002971.
Haberle, R. M., C. B. Leovy, and J. B. Pollack (1982), Some effects of global dust storms on the atmospheric circulation of Mars, *Icarus*, *50*(2–3), 322–367.
Hagen, L. J., and L. Lyles (1988), Estimating small grain equivalents of shrub dominated rangeland for wind erosion control, *Trans. ASAE*, *31*(3), 769–775.
Hamilton, V., H. McSween Jr., and B. Hapke (2005), Mineralogy of Martian atmospheric dust inferred from thermal infrared spectra of aerosols, *J. Geophys. Res.*, *110*, E12006, doi:10.1029/2005JE002501.
Heavens, N. G., M. I. Richardson, and A. D. Toigo (2008), Two aerodynamic roughness maps derived from Mars Orbiter Laser Altimeter (MOLA) data and their effects on boundary layer properties in a Mars general circulation model (GCM), *J. Geophys. Res.*, *113*, E02014, doi:10.1029/2007JE002991.
Heet, T. L., R. E. Arvidson, S. C. Cull, M. T. Mellon, and K. D. Seelos (2009), Geomorphic and geologic settings of the Phoenix Lander mission landing site, *J. Geophys. Res.*, *114*, E00E04, doi:10.1029/2009JE003416.
Holstein-Rathlou, C., et al. (2010), Winds at the Phoenix landing sites, *J. Geophys. Res.*, *115*, E00E18, doi:10.1029/2009JE003411.
Iversen, J. D., and B. R. White (1982), Saltation threshold on Earth, Mars and Venus, *Sedimentology*, *29*, 111–119.
Iversen, J. D., R. Greeley, and J. B. Pollack (1976), Windblown dust on Earth, Mars and Venus, *J. Atmos. Sci.*, *33*, 2425–2429.
Jarvis, P. G., G. B. James, and J. J. Landsberg (1976), Coniferous forests, in *Vegetation and the Atmosphere*, vol. 2, *Case Studies*, edited by J. L. Monteith, pp. 171–240, Academic, London.
Kahre, M. A., J. R. Murphy, R. M. Haberle, F. Montmessin, and J. Schaeffer (2005), Simulating the Martian dust cycle with a finite surface dust reservoir, *Geophys. Res. Lett.*, *32*, L20204, doi:10.1029/2005GL023495.
Kahre, M. A., J. R. Murphy, and R. M. Haberle (2006), Modeling the Martian dust cycle and surface dust reservoirs with the NASA Ames general circulation model, *J. Geophys. Res.*, *111*, E06008, doi:10.1029/2005JE002588.
Kahre, M. A., J. R. Murphy, and R. M. Haberle (2008), Investigations of the variability of dust particle sizes in the Martian atmosphere using the NASA Ames General Circulation Model, *Icarus*, *195*(2), 576–597.
King, J., W. G. Nickling, and J. A. Gillies (2005), Representation of vegetation and other nonerodible elements in aeolian shear stress partitioning models for predicting transport threshold, *J. Geophys. Res.*, *110*, F04015, doi:10.1029/2004JF000281.
Kreslavsky, M. A., and J. W. Head (2000), Kilometer-scale roughness of Mars: Results from MOLA data analysis, *J. Geophys. Res.*, *105*(E11), 26,695–26,711.
Lancaster, N. (2004), Relations between aerodynamic and surface roughness in a hyper-arid cold desert: McMurdo Dry Valleys, Antarctica, *Earth Surf. Processes Landforms*, *29*(7), 853–867.
Lancaster, N., and A. Baas (1998), Influence of vegetation cover on sand transport by wind: Field studies at Owens Lake, California, *Earth Surf. Processes Landforms*, *23*(1), 69–82.
Laurent, B., B. Marticorena, G. Bergametti, P. Chazette, F. Maignan, and C. Schmechtig (2005), Simulation of the mineral dust emission frequencies from desert areas of China and Mongolia using an aerodynamic roughness length map derived from the POLDER/ADEOS 1 surface products, *J. Geophys. Res.*, *110*, D18S04, doi:10.1029/2004JD005013.
Laurent, B., B. Marticorena, G. Bergametti, J. F. Leon, and N. M. Mahowald (2008), Modeling mineral dust emissions from the Sahara Desert using new surface properties and soil database, *J. Geophys. Res.*, *113*, D14218, doi:10.1029/2007JD009484.
Lettau, H. (1969), Note on aerodynamic roughness-parameter estimation on the basis of roughness-element description, *J. Appl. Meteorol.*, *8*, 828–832.
Li, L., and L. W. Martz (1994), Systems of numeric models for sand particle transport by wind, *J. Geophys. Res.*, *99*(D6), 12,999–13,012.
Malin, M. C. (1988), Rock populations as indicators of geologic processes, *NASA Tech. Memo.*, *TM-4041*, 502–504.
Malin, M. C., and K. S. Edgett (2001), Mars Global Surveyor Mars Orbiter Camera: Interplanetary cruise through primary mission, *J. Geophys. Res.*, *106*(E10), 23,429–23,570.
Marshall, J. K. (1971), Drag measurements in roughness arrays of varying density and distribution, *Agric. Meteorol.*, *8*(4–5), 269–292.
Marticorena, B., and G. Bergametti (1995), Modeling the atmospheric dust cycle. 1. Design of a soil-derived dust emission scheme, *J. Geophys. Res.*, *100*(D8), 16,415–16,430.
Marticorena, B., G. Bergametti, B. Aumont, Y. Callot, C. Ndoume, and M. Legrand (1997), Modeling the atmospheric dust cycle 2. Simulation of Saharan dust sources, *J. Geophys. Res.*, *102*(D4), 4387–4404.
Marticorena, B., P. Chazette, G. Bergametti, F. Dulac, and M. Legrand (2004), Mapping the aerodynamic roughness length of desert surfaces from the POLDER/ADEOS bi-directional reflectance product, *Int. J. Remote Sens.*, *25*(3), 603–626.
Marticorena, B., et al. (2006), Surface and aerodynamic roughness in arid and semiarid areas and their relation to radar backscatter coefficient, *J. Geophys. Res.*, *111*, F03017, doi:10.1029/2006JF000462.
Martin, L. J. (1974), The major Martian dust storms of 1971 and 1973, *Icarus*, *23*(1), 108–115.
Martin, L. J. (1976), The 1973 dust storm on Mars: Maps from hourly photographs, *Icarus*, *29*(3), 363–380.
Martin, T. Z. (1995), Mass of dust in the Martian atmosphere, *J. Geophys. Res.*, *100*(E4), 7509–7512.
Mellon, M. T., B. M. Jakosky, H. H. Kieffer, and P. R. Christensen (2000), High-resolution thermal inertia mapping from the Mars Global Surveyor Thermal Emission Spectrometer, *Icarus*, *148*(2), 437–455.
Menenti, M., and J. C. Ritchie (1994), Estimation of effective aerodynamic roughness of Walnut Gulch watershed with laser altimeter measurements, *Water Resour. Res.*, *30*(5), 1329–1337.
Milkovich, S. M., S. Byrne, and P. S. Russell (2010), Quantitative mapping of surface texture on the northern polar residual cap of Mars, Abstract P53F-05 presented at 2010 Fall Meeting, AGU, San Francisco, Calif., 13–17 Dec.
Minvielle, F., B. Marticorena, D. A. Gillette, R. E. Lawson, R. Thompson, and G. Bergametti (2003), Relationship between the aerodynamic roughness length and the roughness density in cases of low roughness density, *Environ. Fluid Mech.*, *3*, 249–267.
Moore, H. J., and B. M. Jakosky (1989), Viking landing sites, remote-sensing observations, and physical-properties of Martian surface materials, *Icarus*, *81*(1), 164–184.
Moore, H. J., and J. M. Keller (1990), Surface-material maps of the Viking landing sites on Mars, *NASA Tech. Memo*, *TM-4210*, 533–535.
Moore, H. J., and J. M. Keller (1991), Surface-material maps of the Viking landing sites on Mars, *NASA Tech. Memo*, *TM-4300*, 60–162.
Moore, H. J., C. R. Spitzer, K. Z. Bradford, P. M. Cates, R. W. Shorthill, and R. E. Hutton (1979), Sample fields of the Viking landers, physical properties, and aeolian processes, *J. Geophys. Res.*, *84*(B14), 8365–8377.
Murphy, J. R., J. B. Pollack, R. M. Haberle, C. B. Leovy, O. B. Toon, and J. Schaeffer (1995), Three-dimensional numerical simulation of Martian global dust storms, *J. Geophys. Res.*, *100*(E12), 26,357–26,376.
Musick, H. B., and D. A. Gillette (1990), Field evaluation of relationships between a vegetation structural parameter and sheltering against wind erosion, *Land Degrad. Rehabil.*, *2*, 87–94.
Neumann, G. A., J. B. Abshire, O. Aharonson, J. B. Garvin, X. Sun, and M. T. Zuber (2003), Mars Orbiter Laser Altimeter pulse width measurements and footprint-scale roughness, *Geophys. Res. Lett.*, *30*(11), 1561, doi:10.1029/2003GL017048.
Newman, C. E., S. R. Lewis, P. Read, and F. Forget (2002a), Modeling the Martian dust cycle: 1. Representations of dust transport processes, *J. Geophys. Res.*, *107*(E12), 5123, doi:10.1029/2002JE001910.
Newman, C. E., S. R. Lewis, P. L. Read, and F. Forget (2002b), Modeling the Martian dust cycle: 2. Multiannual radiatively active dust transport simulations, *J. Geophys. Res.*, *107*(E12), 5124, doi:10.1029/2002JE001920.
Newman, C. E., S. Lewis, and P. Read (2005), The atmospheric circulation and dust activity in different orbital epochs on Mars, *Icarus*, *174*(1), 135–160.
Nickling, W. G., and J. A. Gillies (1989), *Paleoclimatology and Paleometeorology: Modern and Past Patterns of Global Atmospheric Transport*, pp. 133–165, Springer, Dordrecht, Netherlands.
Nowicki, S. A., and P. R. Christensen (2007), Rock abundance on Mars from the Thermal Emission Spectrometer, *J. Geophys. Res.*, *112*, E05007, doi:10.1029/2006JE002798.
Priestley, C. (1959), *Turbulent Transfer in the Lower Atmosphere*, Univ. of Chicago Press, Chicago, Ill.
Putzig, N. E., and M. T. Mellon (2007), Apparent thermal inertia and the surface heterogeneity of Mars, *Icarus*, *191*(1), 68–94.
Raupach, M. R. (1991), Saltation layers, vegetation canopies and roughness lengths, *Acta Mech.*, *1*, 83–96.

Raupach, M. R. (1992), Drag and drag partition on rough surfaces, *Boundary Layer Meteorol.*, *60*(4), 375–395.
Raupach, M. R., A. S. Thom, and I. Edwards (1980), A wind-tunnel study of turbulent flow close to regularly arrayed rough surfaces, *Boundary Layer Meteorol.*, *18*, 373–397.
Raupach, M. R., D. A. Fillette, and J. F. Leys (1993), The effect of roughness elements on wind erosion, *J. Geophys. Res.*, *98*(D2), 3023–3029.
Richardson, M. I., A. D. Toigo, and C. E. Newman (2007),PlanetWRF: A general purpose, local to global numerical model for planetary atmospheric and climate dynamics, *J. Geophys. Res.*, *112*, E09001, doi:10.1029/2006JE002825.
Schlicting, H. (1936), Experimentelle Untersuchungen zum Rauhigkeitsproblem, *Arch. Appl. Mech. Ing.-Arch.*, *7*(1), 1–34.
Shao, Y. P. (2001), A model for mineral dust emission, *J. Geophys. Res.*, *106*(D17), 20,239–20,254.
Shao, Y. P., M. R. Raupach, and P. A. Findlater (1993), Effect of saltation bombardment on the entrainment of dust by wind, *J. Geophys. Res.*, *98*(D7), 12,719–12,726.
Shao, Y. P., M. R. Raupach, and J. F. Leys (1996), A model for predicting aeolian sand drift and dust entrainment on scales from paddock to region, *Aust. J. Soil. Res.*, *34*(3), 309–342.
Spiga, A., and S. Lewis (2010), Martian mesoscale and microscale wind variability of relevance for dust lifting, *Mars*, *5*, 146–158.
Sullivan, R., R. Greeley, M. Kraft, G. Wilson, M. Golombek, K. Herkenhoff, J. Murphy, and P. Smith (2000), Results of the Imager for Mars Pathfinder windsock experiment, *J. Geophys. Res.*, *105*(E10), 24,547–24,562.
Sutton, J. L., C. B. Leovy, and J. E. Tillman (1978), Diurnal variations of the Martian surface layer meteorological parameters during the first 45 sols at two Viking lander sites, *J. Atmos. Sci.*, *35*(12), 2346–2355.
Westphal, D. L., O. B. Toon, and T. N. Carlson (1987), A two-dimensional numerical investigation of the dynamics and microphysics of Saharan dust storms, *J. Geophys. Res.*, *92*(D3), 3027–3049.
Whelley, P. L., and R. Greeley (2008), The distribution of dust devil activity on Mars, *J. Geophys. Res.*, *113*, E07002, doi:10.1029/2007JE002966.
White, B. R. (1979), Soil transport by winds on Mars, *J. Geophys. Res.*, *84*(B9), 4643–4651.
White, B. R., B. M. Lacchia, R. Greeley, and R. N. Leach (1997), Aeolian behavior of dust in a simulated Martian environments, *J. Geophys. Res.*, *102*(E11), 25,629–25,640.
Wilson, R. J. (1997), A general circulation model simulation of the Martian polar warming, *Geophys. Res. Lett.*, *24*(2), 123–126.
Wilson, R. J., and K. Hamilton (1996), Comprehensive model simulation of thermal tides in the Martian atmosphere, *J. Atmos. Sci.*, *53*(9), 1290–1326.
Wolfe, S., and W. G. Nickling (1996), Shear stress partitioning in sparsely vegetated desert canopies, *Earth Surf. Processes Landforms*, *21*(7), 607–619.
Wyatt, V., and W. G. Nickling (1997), Drag and shear stress partitioning in sparse desert creosote communities, *Can. J. Earth Sci.*, *34*(11), 1486–1498.
Yingst, R. A., A. F. C. Haldemann, K. L. Biedermann, and A. M. Monhead (2007), Quantitative morphology of rocks at the Mars Pathfinder landing site, *J. Geophys. Res.*, *112*, E06002, doi:10.1029/2005JE002582.
Zender, C. S., R. L. Miller, and I. Tegen (2004), Quantifying mineral dust mass budgets: Terminology, constraints, and current estimates, *Eos Trans. AGU*, *85*(48), 509–512.
Zurek, R. W. (1982), Martian great dust storms: An update, *Icarus*, *50*(1–2), 288–310.
Zurek, R. W., and L. J. Martin (1993), Interannual variability of planet-encircling dust storms on Mars, *J. Geophys. Res.*, *98*(E2), 3247–3259.

G. Bergametti, P. Coll, and B. Marticorena, LISA, UMR CNRS 7583, Université Paris Est Créteil et Université Paris Diderot, Institut Pierre Simon Laplace, C.M.C., 61 ave. du Gènèral de Gaulle, F-94010 Créteil CEDEX, France.

F. Forget, LMD, UMR CNRS 8539, Université Pierre et Marie Curie, Institut Pierre Simon Laplace, 4 pl. Jussieu, BP 99, F-75252 Paris CEDEX 05, France.

E. Hébrard, LAB, UMR CNRS 5804, Université Bordeaux 1, Observatoire Aquitain des Sciences de l'Univers, 2 rue de l'Observatoire, BP 89, F-33271 Floirac CEDEX, France. (hebrard@obs.u-bordeaux1.fr)

C. Listowski, A. Määttänen, and F. Montmessin, LATMOS, UMR CNRS 8190, Université de Versailles Saint Quentin en Yvelines et Université Pierre et Marie Curie, Institut Pierre Simon Laplace, 11 blvd. d'Alembert, Quartier des Garennes, F-78280 Guyancourt, France.